

## Article

# Fusion of Remote Sensing Data Using GIS-Based AHP-Weighted Overlay Techniques for Groundwater Sustainability in Arid Regions

Mohamed Abdekareem <sup>1,2,\*</sup> , Nasir Al-Arifi <sup>3,\*</sup>, Fathy Abdalla <sup>1,4</sup> , Abbas Mansour <sup>1</sup> and Farouk El-Baz <sup>5</sup>

<sup>1</sup> Geology Department, South Valley University, Qena 83523, Egypt; fabdalla@ksu.edu.sa (F.A.); aman@svu.edu.eg (A.M.)

<sup>2</sup> Remote Sensing Lab, South Valley University, Qena 83523, Egypt

<sup>3</sup> Chair of Natural Hazards and Mineral Resources, Geology and Geophysics Department, King Saud University, Riyadh 11451, Saudi Arabia

<sup>4</sup> Scientific Research Chairs Program, King Saud University, Riyadh 11451, Saudi Arabia

<sup>5</sup> Center for Remote Sensing, Boston University, 725 Commonwealth Ave., Boston, MA 02215, USA; farouk@bu.edu

\* Correspondence: mohamed.abdelkareem@sci.svu.edu.eg (M.A.); nalarifi@ksu.edu.sa (N.A.-A.)

**Abstract:** Remote sensing and GIS approaches have provided valuable information on modeling water resources, particularly in arid regions. The Sahara of North Africa, which is one of the driest regions on Earth, experienced several pluvial conditions in the past that could have stored significant amounts of groundwater. Thus, harvesting the stored water by revealing the groundwater prospective zones (GWPZs) is highly important to water security and the management of water resources which are necessary for sustainable development in such regions. The Shuttle Radar Topography Mission (SRTM) digital elevation model (DEM), Advanced Land Observing Satellite (ALOS)/Phased Array type L-band Synthetic Aperture Radar (PALSAR), Tropical Rainfall Measuring Mission (TRMM), and Landsat-8 OLI data have all successfully revealed the geologic, geomorphic, climatic, and hydrologic features of Wadi El-Tarfa east of Egypt's Nile River. The fusion of eleven predictive GIS maps including lithology, radar intensity, lineament density, altitude, slope, depressions, curvature, topographic wetness index (TWI), drainage density, runoff, and rainfall data, after being ranked and normalized through the GIS-based analytic hierarchy process (AHP) and weighted overlay methods, allowed the GWPZs to be demarcated. The resulting GWPZs map was divided into five classes: very high, high, moderate, low, and very low potentiality, which cover about 10.32, 24.98, 30.47, 24.02, and 10.20% of the entire basin area, respectively. Landsat-8 and its derived NDVI that was acquired on 15 March 2014, after the storm of 8–9 March 2014, along with existing well locations validated the GWPZs map. The overall results showed that an integrated approach of multi-criteria through a GIS-based AHP has the capability of modeling groundwater resources in arid regions. Additionally, probing areas of GWPZs is helpful to planners and decision-makers dealing with the development of arid regions.

**Keywords:** remote sensing; GIS; modeling; groundwater; arid regions; Wadi El-Tarfa



**Citation:** Abdekareem, M.; Al-Arifi, N.; Abdalla, F.; Mansour, A.; El-Baz, F. Fusion of Remote Sensing Data Using GIS-Based AHP-Weighted Overlay Techniques for Groundwater Sustainability in Arid Regions. *Sustainability* **2022**, *14*, 7871. <https://doi.org/10.3390/su14137871>

Academic Editor: Daniela Baldantoni

Received: 27 April 2022

Accepted: 23 June 2022

Published: 28 June 2022

**Publisher's Note:** MDPI stays neutral with regard to jurisdictional claims in published maps and institutional affiliations.



**Copyright:** © 2022 by the authors. Licensee MDPI, Basel, Switzerland. This article is an open access article distributed under the terms and conditions of the Creative Commons Attribution (CC BY) license (<https://creativecommons.org/licenses/by/4.0/>).

## 1. Introduction

Groundwater is a natural resource that is necessary for sustaining life, particularly in arid/hyper-arid zones, which are characterized by a scarcity of rainfall and surface water [1,2]. Securing additional water resources in such areas of severe climatic conditions is necessary due to the increase of the population and economic activities [2–5]. This is because the lack of rainfall and surface water in the Saharan countries requires exploring new water resources. This also includes Egypt, which will probably suffer from water deficiencies in the future if it does not find additional water resources [2]. Hence, mapping

groundwater potential zones (GWPZs) is essential to afford water security in residential areas and other localities [6,7]. Increase in the demand for freshwater worldwide calls for revealing new water resources through applying geological, geophysical, and remote sensing techniques. It is a great challenge to secure additional source of waters as they relate to climatic, hydrologic, and topographic conditions [8]. Climate change has been noticeably realized worldwide [9,10] and it impacts the spatial distribution of rainfall intensity, as climate conditions and geomorphic and physical characteristics of the catchments [11–13] control the occurrence of water resources.

Since the first launching of the Earth Resources Technology Satellite (ERTS-1) in July 1972, which was later named Landsat-1, advances have been achieved in exploring and monitoring the Earth's resources. Optical and microwave satellite remote sensing (SRS) data provided precious data for revealing and predicting prospective areas of water resources in different environmental conditions around the world [14–19]. The progress in SRS allowed different features of the hydrological conditions to be probed [20] and promising areas of water resources to be predicted using multi-criteria [3]. Synthetic aperture radar (SAR) microwave remote sensing data are essential to revealing hidden geologic features, fluvial deposits, and hidden paleochannels that were masked by sand deposits [6,21,22]. Radar waves have an ability to image the desert surface at any time irrespective of weather conditions and proved to be a significant approach in characterizing the past fluvial deposits which were masked by sand sheets and dunes before further field investigations [1], as radar waves have the capability to probe the subsurface to the depth of many meters [23,24]. Several studies successfully applied radar data, e.g., Radarsat-1, ALOS/PALSAR, and SRTM, in finding water resources [2,6,7].

The knowledge-driven analytic hierarchy process (AHP) method [25,26], based on geographic information systems (GIS) and weighted overlay analysis, are tested in the present study to generate a GWPZs map. The hierarchical tree of different levels includes purpose, criteria, and choices, and its level of criteria is divided into various sub-criteria [4]. This kind of multi-criteria decision-making approach has been widely applied in several predictive studies [4,5,18,19,27,28] to find a solution for complex decision analysis depending on ordering criteria in hierarchical orders [5].

Several geomorphic, geologic, and hydrologic factors, e.g., lithology, geologic structures, altitude, slope, drainage density, rainfall, and runoff, influence the existence of groundwater and aid in finding GWPZs [2,15,17,29]. Fusion of these multi-evidential layers (derived from remote sensing and conventional maps through GIS approaches) has facilitated predicting the prospective sectors for GWPZs, characterizing infiltration and recharging capacity, and revealing the best areas for well-abstraction [17,30–32].

Lithologic characteristics control the permeability and porosity, which hold groundwater and influence infiltration capacity [3,7,33]. Formations of high permeability and porosity induce the percolation and recharging of water into the aquifers below. On the other hand, impermeable massive rocks promote surface runoff [6,34]. Moreover, lineaments, including faults/fracture zones, represent the conduits of water flow between the surface and subsurface strata. They reveal below lithologic and geomorphic features that have positive relationships to the occurrence of groundwater [35]. In addition, the altitude is also an important index of controlling the occurrence of the groundwater as it is widely employed in mapping GWPZs [2,36] and is extremely necessary for groundwater prospection studies. The areas of low elevations are positively related to infiltration, particularly depression areas [2,7]. The variation in elevations generates slope, which is an important factor in controlling the runoff, and infiltration capacity for revealing GWPZs due to its indication of the gradient in the elevations of the catchments [8,13], the speed of runoff, and infiltration capabilities [2,8]. Moreover, land surface curvature represents the morphology of the land surface, which is an important factor that is connected to accumulation, infiltration, and runoff on the slope [8,37,38]. The topographic wetness index (TWI) is also utilized to evaluate topographic influences in understanding hydrological conditions. The TWI was presented by Moore et al. [39]. The physical properties of the catchments and the

density of drainage networks provide effective information regarding the infiltration and runoff characteristics of precipitated water during heavy rainfall [7,30,40]. The quantitative morphometric parameters derived from the Shuttle Radar Topography Mission (SRTM) digital elevation model (DEM) data [2,12,41] also present valuable information regarding the geometry, texture, and relief of the morphometric characteristics of the basins that control the runoff and infiltration capacity and thus the occurrence of groundwater.

Despite the fact that integrating remote sensing and GIS-based mapping of groundwater quality is beneficial for sustainable development, only a few studies have been conducted to evaluate groundwater occurrences in arid regions. However, few published works in Egypt's deserts have used geospatial and statistical modelling techniques in conjunction with GIS. Furthermore, the impact of geological, extracted depressions and morphometric-geomorphic characteristics on groundwater occurrences has received little attention.

The present study aimed to (1) test the knowledge-driven GIS-based AHP technique for preparing, normalizing, and fusing various groundwater-related factors derived from remote sensing data using overlay techniques to delineate accurately and effectively the prospective areas of groundwater; (2) characterize the hydrologic, climatic, geologic, and morphometric characteristics of the catchments using optical and radar remote sensing data; and (3) test the use of SRTM DEM-related parameters as model inputs for modeling groundwater potential zones in an arid area of the eastern Sahara using remote sensing data and GIS-based AHP.

## 2. Study Area

The area of Wadi El-Tarfa (W. El-Tarfa) occurs east of the northern section of the Nile; it drains westward to the Nile at El-Minya and catches the rainwater from the highlands to the east during rainstorms. The W. El-Tarfa catchment area covers ~10,605 km<sup>2</sup> that stretches between latitudes 27°31'10" to 37°31'41" N and longitudes 30°50'00" to 32°29'26" E (Figure 1a,b). It is covered by a Cretaceous/Tertiary sedimentary sequence with small exposures of Paleozoic that unconformably overlay the basement rocks to the east. The Paleozoic–Lower Tertiary sediments consist of different varieties of sandstone, shale, and carbonates that are intercalated with chalk and shale. The oldest sedimentary rock in the present basin is the Samr el-Qa Formation (Figure 2a,b belongs to Lower Carboniferous and consists of fluvial sandstone with marine intercalation) [42]. It is followed by exposures of Lower Cretaceous sediments, e.g., the Wadi Qena Formation, which mainly consists of fluvial massive white sandstone. These formations are followed by Upper Cretaceous/Paleocene sediments which comprise fluvial and marine sediments of marl, shale, and chalky limestone. The Eocene rocks built-up of two groups. Thebes and Mokattam, consist of thinly bedded chalk, chalky limestone rich in cherty bands, and open marine limestone and marl intercalated with clay and shale. The wadi bed is covered by Quaternary wadi deposits as the wadi is incised through the Ma'aza plateau that is capped by hard massive limestone [42]. These deposits are sand, gravel, and fanglomerate that are derived from weathering and erosion of the pre-existing rocks. Structurally, the area is shaped by the uplift from the northeast and dominated by NW-SE and NE-SW trends. Hydrologically, the area is situated in an arid environment that receives a lesser amount of rainfall during the year (Figure 1a) that drains the Nile River in recharging the groundwater aquifers of W. El-Tarfa.

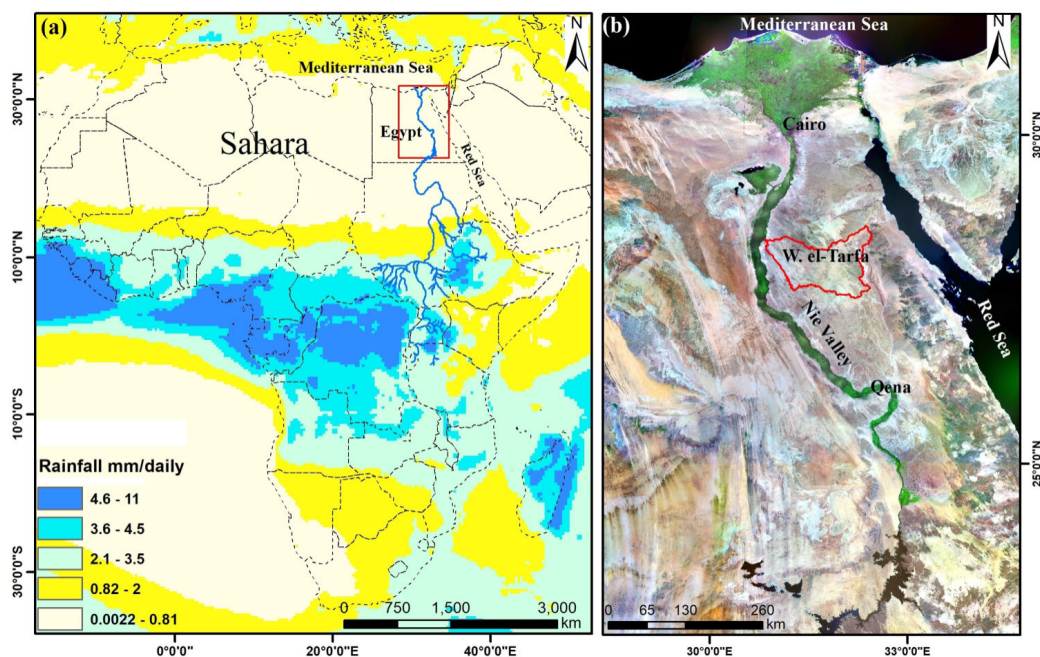


Figure 1. Location maps: (a) rainfall distribution map of Africa, which displays the arid conditions of the Great Sahara, and (b) Landsat mosaic of Egypt overlain by W. El-Tarfa basin in a red polygon.

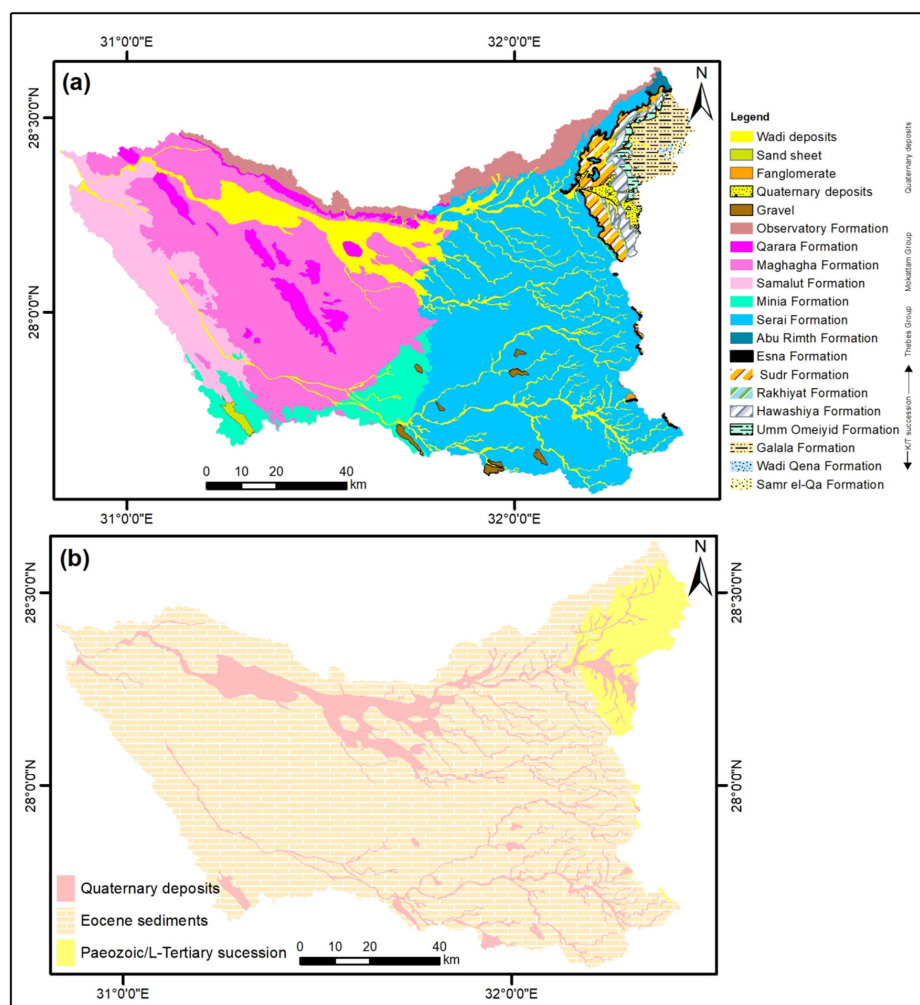


Figure 2. (a) Geologic map (1987) of Wadi El-Tarfa and (b) simplified geologic map.

### 3. Data Used and Methods

Several satellite radar and optical data were collected to characterize the prospective area of groundwater in the W. El-Tarfa basin. The SRTM DEM data were selected to map the topographic characteristics and compute the catchment's parameters. Landsat-8 Operational Land Imager (OLI) data were also utilized to validate the GWPZs (Figure 3).

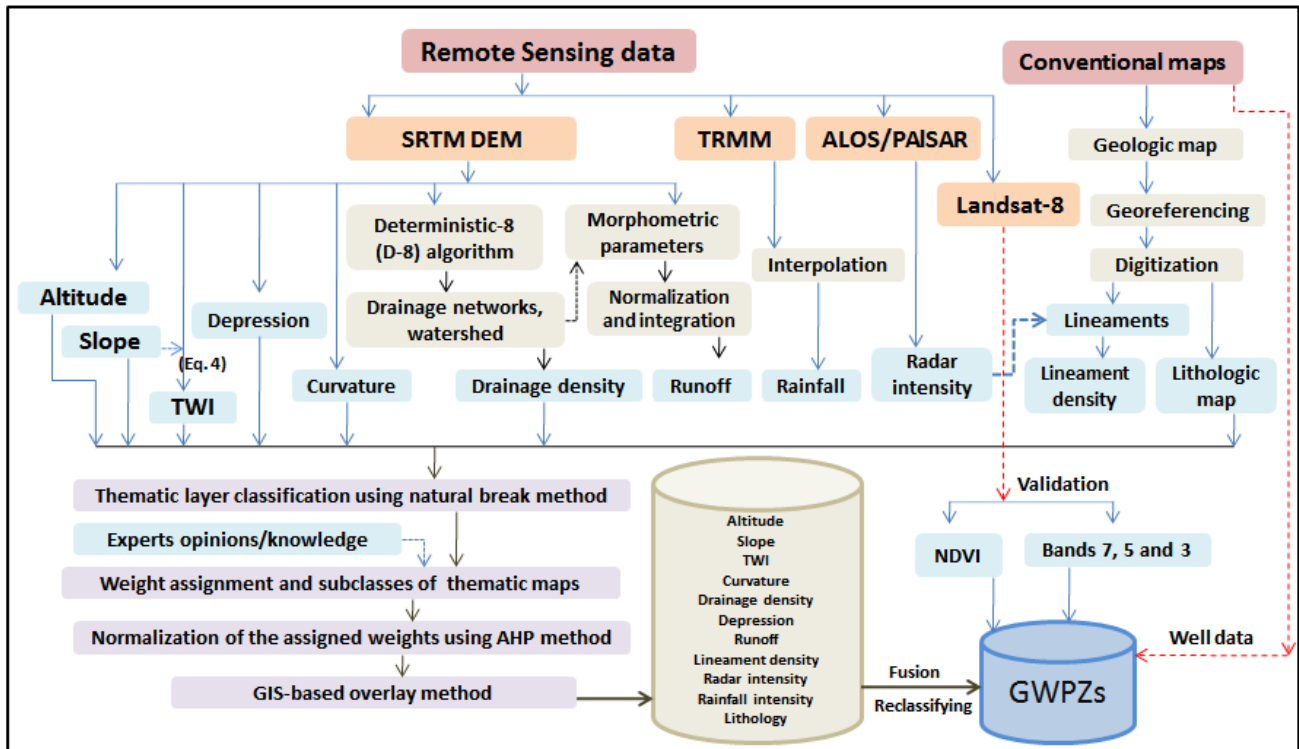


Figure 3. Flow chart displays the data used and methods included in revealing GWPZs.

The SRTM DEM data (~90 m cell size) were obtained as an international collaboration between NASA, the U.S. National Geospatial-Intelligence Agency, the Italian Space Agency, and the German Aerospace Center. The SRTM DEM data are available for download from the U.S. Geological Survey (USGS). These data were utilized to delineate the watershed, drainage networks, altitude, slope, surface curvature, topographic wetness index (TWI), depressions, stream density, and morphometric parameters. The latter parameters, such as bifurcation ratio, elongation ratio, form factor, circularity ratio, drainage texture, stream frequency, drainage density, length of overland flow, infiltration number, basin relief, relief ratio, and ruggedness (Appendices A and B), were calculated using the mathematical formula as depicted in the literature of Abdelkareem [15]. The Deterministic-8 (D-8) algorithm [43] was used to perform the automatic delineation of stream extractions. The stream orders were identified [44,45] and used to calculate other parameters.

The Landsat Operational Land Imager (OLI) optical sensor with 9 spectral bands carried by Landsat-8 was launched on 11 February 2013. Two scenes of Level 1 (175/041 and 176/040) OLI data were acquired on 24 March 2014, and 15 March 2014. The obtained scenes were mosaicked and linked to the coordinate system of UTM Zone 37 N. The Landsat-8 OLI was employed here to perform image transformation and enhancement approaches such as composite bands 7, 5, and 3 to reveal water signatures in cyan and vegetated areas using the normalized difference vegetation index (NDVI). This index is calculated using the visible infrared bands of the Landsat satellite:  $NDVI = \frac{NIR \text{ (band 5)} - R \text{ (band 4)}}{NIR \text{ (band 5)} + R \text{ (band 4)}}$ . The high values close to +1 (white tone) of NDVI refer to vegetated areas while low values close to -1 (dark tone) indicate probable water signatures [5,46]. In the present study, NDVI values of the wet areas that display evidence

of water signatures range from  $-0.015$  to  $0.07$ , and the vegetated areas range from  $0.11$  to  $0.55$ .

The presented GIS-based model is primarily based on topography (e.g., altitude, slope, depressions, and curvature), hydrologic (TWI and drainage density), climatic (rainfall), and morphometric (runoff) parameters along with geological data including lithologic units and lineaments that were derived and digitized from the geological map of Conoco [42]. The hillshade and extracted drainage networks derived from the SRTM DEM were also utilized in digitizing the lineaments. Mapping GWPZ susceptible areas requires complex data sets to characterize the catchment properties to get the output map. Modeling of GWPZs requires more information.

ALOS/PALSAR-2, an advanced Japanese land observation satellite equipped with a radar sensor and the forerunner of the JAXA L-SAR device launched in 2014, is an active microwave sensor with an incident angle ranging from  $8^\circ$  to  $70^\circ$  [47]. It operates on the L-band ( $1257.5$  MHz;  $= 22.9$  cm). Within 24 h, the devices are widely used for land observation in all meteorological conditions. The JAXA PALSAR mosaic “PALSAR-2 Global Forest/Non-forest 2017 Map” was used in this study due to the large study area [48]. The data were preprocessed and are available in two polarizations (HH and HV). This research makes use of HH polarization, which is used for direct viewing. A subset of ALOS/PALSAR-2 mosaic with a seamless global of 25 m spatial resolution was extracted using the Wadi El-Tarfa watershed and employed to distinguish the fine-grained deposits in a dark tone due to specular reflection from the rough surface and bed rocks in white [49].

The average rainfall data was acquired from TRMM satellite records. The obtained average rainfall data cover the period between 1 January 1998 and 30 November 2015 and many discontinuous storms on 29 December 2010, 17 to 18 January 2010, 8 to 9 March 2014, and in 2015. The data are available at the following website: <https://giovanni.gsfc.nasa.gov/giovanni/> (accessed on 10 February 2021).

The applied knowledge-driven AHP model in the present study is based on parameters derived from remote sensing, e.g., topographic, hydrologic, climatic, and geologic data, and the relative importance of each observation is decided on by the user. The GIS approach uses the raster combination in which each pixel of each layer has the same geographic location. This makes the combination process more appropriate for integrating characteristics of several data sets into an output layer.

In this model, the weighted values are given to the spatial predictor maps and their categories (sub-classes). The thematic layers' control factor of groundwater occurrence, interactions, and precipitations are weighted corresponding to Saaty's (1–9) scale [26]. A numeric value given to each layer ( $L_i$ ) promotes the synergetic method and gives a new grade to each pixel in the output cell. A high value, e.g., 9, indicates extreme probability, but, e.g., 2 and 1 indicate weak to equal importance, 3 indicates moderate importance, 4 indicates moderate plus, 5 indicates strong importance, 6 indicates strong plus, 7 indicates very to extreme importance, and 8 indicates very-very strong, respectively [26]. Subsequently, the predictor layers have been matched with each other in a pair wise comparison matrix (Table 1) that allows ordering and organizing criteria in hierarchical order to calculate consistency ratio (Table 2). Moreover, the sub-classes of each layer are given a weight ( $F_i$ ) based on their relative importance given by the users based on their knowledge and opinions in predicting the water resources through using the natural breaks re-classification method (Table 3). Subsequently, each sub-class is correlated and normalized to its counterparts (Table 3), for example, in Table 3 the sub-class of very high lineament density is given a weight of “7” but the very low is given a “2”. The uncertainty in this approach can be assessed through the principal eigenvalue and consistency index (CI). In this model, calculating the consistency ratio (CR) can be accomplished (Table 2) by determining the principal eigenvalue ( $\lambda$ ) that was computed by the eigenvector approach and consistency index (CI). The latter can be computed from the following equation:

$$CI = \frac{(\lambda_{max} - 1)}{(n - 1)} \quad (1)$$

where  $\lambda_{max}$  represents the principal eigenvalue and  $n$  is the number of factors.

$$CR = \frac{CI}{RCI} \tag{2}$$

where RCI = random consistency index value, whose values were obtained from Saaty’s standard:

$$CI = \frac{(11 - 11)}{(11 - 1)} = 0 \tag{3}$$

The CR of the present study is  $0/1.51 = 0$ , that is, acceptable for conducting the analysis as a CR of 0.10 or less is acceptable to continue the analysis [28,50] as it measures the consistency between the pair wise comparison matrix.

**Table 1.** Pair wise matrix of eleven indices.

	Litho	Rad	Lin	Top	Dep	Sl	Cur	TWI	Dd	Ruf	Rain
Litho	1.00	0.71	0.83	0.83	0.71	0.71	1.25	1.00	1.00	1.25	0.83
Rad	1.40	1.00	1.17	1.17	1.00	1.00	1.75	1.40	1.40	1.75	1.17
Lin	1.20	0.86	1.00	1.00	0.86	0.86	1.50	1.20	1.20	1.50	1.00
Top	1.20	0.86	1.00	1.00	0.86	0.86	1.50	1.20	1.20	1.50	1.00
Dep	1.40	1.00	1.17	1.17	1.00	1.00	1.75	1.40	1.40	1.75	1.17
Sl	1.40	1.00	1.17	1.17	1.00	1.00	1.75	1.40	1.40	1.75	1.17
Cur	0.80	0.57	0.67	0.67	0.57	0.57	1.00	0.80	0.80	1.00	0.67
TWI	1.00	0.71	0.83	0.83	0.71	0.71	1.25	1.00	1.00	1.25	0.83
Dd	1.00	0.71	0.83	0.83	0.71	0.71	1.25	1.00	1.00	1.25	0.83
Ruf	0.80	0.57	0.67	0.67	0.57	0.57	1.00	0.80	0.80	1.00	0.67
Rain	1.20	0.86	1.00	1.00	0.86	0.86	1.50	1.20	1.20	1.50	1.00
Sum	12.40	8.86	10.33	10.33	8.86	8.86	15.50	12.40	12.40	15.50	10.33

Abbreviations: Litho—lithology; Rad—radar intensity; Lin—lineaments; Top—altitude; Dep—depression; Sl—slope; Cur—curvature; TWI—topographic wetness index; Dd—drainage density; Ruf—runoff; Rain—rainfall.

**Table 2.** Calculating consistency ratio.

	Litho	Rad	Lin	Top	Dep	Sl	Cur	TWI	Dd	Ruf	Rain	Weighted Sum	Criteria Weights	$\lambda_{max}$
Litho	0.081	0.081	0.081	0.081	0.081	0.081	0.081	0.081	0.081	0.081	0.081	0.887	0.081	11
Rad	0.113	0.113	0.113	0.113	0.113	0.113	0.113	0.113	0.113	0.113	0.113	1.242	0.113	11
Lin	0.097	0.097	0.097	0.097	0.097	0.097	0.097	0.097	0.097	0.097	0.097	1.065	0.097	11
Top	0.097	0.097	0.097	0.097	0.097	0.097	0.097	0.097	0.097	0.097	0.097	1.065	0.097	11
Dep	0.113	0.113	0.113	0.113	0.113	0.113	0.113	0.113	0.113	0.113	0.113	1.242	0.113	11
Sl	0.113	0.113	0.113	0.113	0.113	0.113	0.113	0.113	0.113	0.113	0.113	1.242	0.113	11
Cur	0.065	0.065	0.065	0.065	0.065	0.065	0.065	0.065	0.065	0.065	0.065	0.710	0.065	11
TWI	0.081	0.081	0.081	0.081	0.081	0.081	0.081	0.081	0.081	0.081	0.081	0.887	0.081	11
Dd	0.081	0.081	0.081	0.081	0.081	0.081	0.081	0.081	0.081	0.081	0.081	0.887	0.081	11
Ruf	0.065	0.065	0.065	0.065	0.065	0.065	0.065	0.065	0.065	0.065	0.065	0.710	0.065	11
Rain	0.097	0.097	0.097	0.097	0.097	0.097	0.097	0.097	0.097	0.097	0.097	1.065	0.097	11

**Table 3.** Evidential factors contorting the occurrence of groundwater.

	Assigned Weight	Sub-Classes	Rank	Grade	Normalized Rank	Area %
Lithology	5	Quaternary deposits	6	High	0.55	11.78
		Eocene sediments	3	Moderate	0.27	82.21
		Paleozoic/L-Tertiary	2	Low	0.18	6.01
Radar intensity	7	22–44	8	Very high	0.44	27.74
		44–85	5	High	0.28	47.18
		85–173	3	Moderate	0.17	21.17
		173–255	2	Low	0.11	3.91
Lineaments (km/km <sup>2</sup> )	6	0–15.27	2	Very low	0.29	14.50
		15.27–27.63	4	Low	0.25	27.51
		27.63–39.27	5	Moderate	0.21	27.30
		39.27–52.73	6	High	0.17	21.45
		52.73–92.73	7	Very high	0.08	9.23
Altitude (m)	6	27–264	8	Very high	0.31	25.45
		264–413	7	High	0.27	24.65
		413–574	5	Moderate	0.19	19.27
		574–736	4	Low	0.15	20.91
		736–1260	2	Very low	0.08	9.71
Depression (m)	7	–31 to –2.64	8	High	0.50	2.64
		–2.64 to –0.72	5	Moderate	0.31	7.42
		–0.72 to 0	3	Low	0.19	89.94
Slope (degree)	7	0–3	5	Very high	0.33	54.72
		3 to 5	4	High	0.27	26.48
		5 to 10	3	Moderate	0.20	14.95
		10 to 15	2	Low	0.13	2.68
		>15	1	Very low	0.07	1.18
Curvature (radians/100 m)	4	–2.66 to –0.0889	2	Low	0.2	25.84
		–0.0889 to 0.139	3	Moderate	0.3	27.11
		0.139 to 2.8339	5	High	0.5	47.05
TWI	5	4.78 to 8.07	1	Very high	0.09	27.92
		8.07 to 9.48	2	High	0.18	41.58
		9.84 to 11.31	3	Moderate	0.27	20.62
		11.31 to 17.69	5	Low	0.45	9.88
		6.55 to 47.79	2	Very low	0.10	9.1
Drainage density (km/km <sup>2</sup> )	5	47.79 to 66.80	3	Low	0.14	22.35
		66.80 to 83.17	4	Moderate	0.19	31.66
		83.17 to 100.60	5	High	0.24	25.39
		100.60 to 141.27	7	Very high	0.33	11.51

Table 3. Cont.

	Assigned Weight	Sub-Classes	Rank	Grade	Normalized Rank	Area %
Runoff	4	24.49–25.95	5	Very high	0.33	10.86
		25.97–29.23	4	High	0.27	23.82
		29.24–33.15	3	Moderate	0.20	33.79
		33.16–40.43	2	Low	0.13	20.91
		40.44–46.87	1	Very low	0.07	10.62
Rainfall (mm/day)	6	0.0120 to 0.0174	2	Low	0.20	70.31
		0.0174 to 0.0307	3	Moderate	0.30	18.08
		0.0307 to 0.0874	5	High	0.50	11.61

In the applied overlay analysis, every pixel of each thematic layer corresponds to the same location. That means it is appropriate to fuse many aspects for the input eleven layers into an output groundwater prospective zones (GWPZs) map. It is worth noting numeric ranks are given to each layer and sub-class, letting the user mathematically fuse the layers and appoint a new rank to each pixel in the output GWPZs map. Thus, in this model, the GWPZs map of the study area which represents the weighted average of the combined data-based maps (multi-criteria) was combined with the minimum inputs cell size (~90 m) in a GIS-based weighted overlay approach using the following equation:

$$\text{GWPZs} = \sum_{i=1}^n L_i \times F_i \quad (4)$$

where  $L_i$  indicates the normalized weight of an evidential layer of the  $i$  parameter and  $F_i$  relates to the power of the inter-map (sub-class) features. This allows all of the eleven thematic maps to be combined on a pixel basis related to the above equation.

#### 4. Factors Influencing GWPZs

##### 4.1. Lithology

The exposed lithologic units that are highly permeable would catch and capture surface water flow versus the impermeable ones. The lithologic map was digitized from the geological map of Conoco [42]. It was classified and normalized as listed in Table 3. The lithological formations of the Wadi El-Tarfa basin area (Figure 1a,b) consist of a plateau of limestone. This belongs to the Mokattam Group of Eocene age that covers the Cretaceous/Tertiary sedimentary succession. The latter is exposed to the east as a result of uplift. The lithologic map is classified into three simple geologic units, viz., Paleozoic-L Tertiary, Eocene sediments, and Quaternary deposits that give weights 2 (low), 3 (moderate), and 6 (high), respectively (Table 3). These units cover 6.01, 82.21, and 11.78%, respectively, of the entire study area (Table 3). The occurrence of Quaternary sand deposits being highly porous yields the recharging capability; thus, they are labeled with high potentiality and are considered to be “high” to “very high” for groundwater recharge.

##### 4.2. Radar Intensity

Using ALOS/PALSAR data (Figure 4a), the alluvial deposits appear in dark tones. These deposits are extremely important in characterizing the prospective locations of GWPZs, as they indicate the amount of water flow during the past hydrologic processes. Moreover, these deposits are characterized by high permeability and porosity, acting as a suitable location for accumulating and storing groundwater [1,6,7]. Thus, areas of sand accumulation would be considered the prime zones of water accumulation as they lose sediments that hold the amount of precipitated water during rainy storms in arid

regions [2,7]. Therefore, the present study classified data, by Arc GIS software (Esri, Redlands, CA, USA) packages, into four zones, viz., low (2), moderate (3), high (5), and very high (8). It is worth noting that the classes from lower to higher potentiality cover 3.91%, 21.17, 47.18, and 27.74% of the entire area (Figure 4b; Table 3).

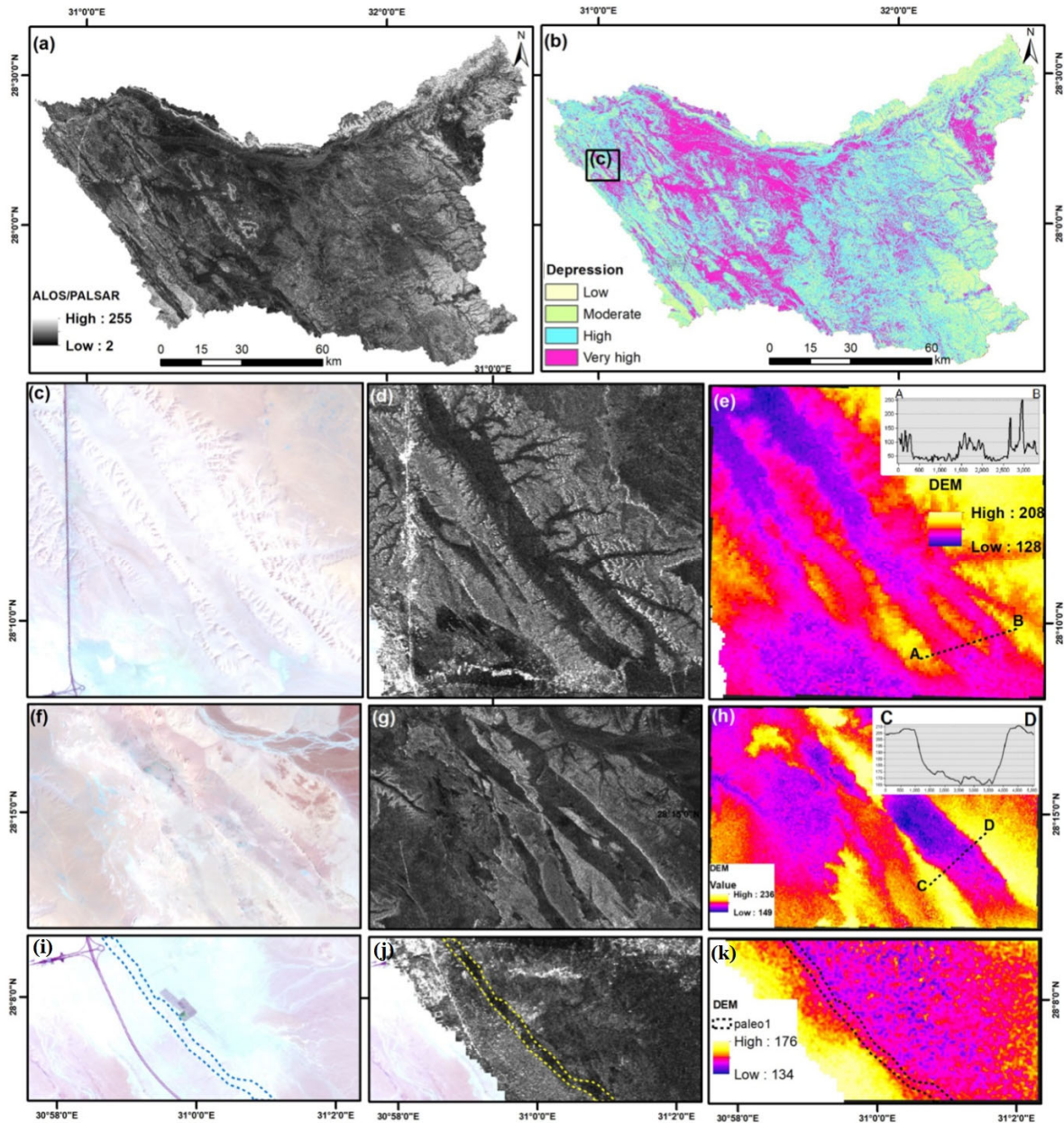


**Figure 4.** Radar data vs. optical Landsat-8 (a) ALOS/PALSAR data displaying the physical characteristics of Wadi El-Tarfa basin and (b) ALOS/PALSAR data classified into four prospective zones; the black polygon refers to the counterpart area in (c). (c,f,i) Subsets of Landsat-8 reveal unrecognized channels filled with alluvial deposits in the downstream area that is clearly recognized in subsets (d,g,j) of ALOS/PALSAR and DEM (e,h,k).

It is worth noting that the ALOS/PALSAR L-band intensity of backscattering data provided interesting information regarding the existence of paleochannels, fluvial deposits, and soil texture, which is a significant factor in recharging and infiltration. Unlike Landsat-8 OLI images (Figure 4c,f,i), radar data unveiled the cover of sand and characterized the dark tone that belongs to fluvial deposits of probable paleochannels (Figure 4d,g,j), which agrees with DEM (Figure 4e,h,k) and is difficult to realize in OLI data (Figure 4c,f,i).

### 4.3. Lineaments

Lineaments induce permeability and secondary porosity and have a valuable task in controlling the recharge potentiality. The lineaments (Figure 5a) were extracted using geological map [42], ALOS/PASAR, SRTM, and Landsat data. Delineating of these lineaments displays that the main trend is NW-SE and NE-SW that they control the wadi. Understanding the density of lineaments is also significant [51]. Lineament density (Figure 5b), is estimated as the lengths of lineament segments in a particular region per its area using Arc GIS software. Most of the areas of high density are located in the eastern part associated with the Thebes Group. The density data of W. El-Tarfa was reclassified into five zones including very low (2), low (4), moderate (5), high (6), and very high (7). The high ranks were assigned to high lineament density based on the dense zones of lineaments, considered the prospective zones of groundwater recharging [4,19] that promote high well yield [52]. The fractures and faults are depicted using DEM and ALOS/PASAR data and topographic profiles (Figure 5c–h). More than 30% of the basin is characterized by high lineament density, which favors the circulation of the precipitated water into the strata below. However, zones of low and very low density characterized 40% (Table 3).

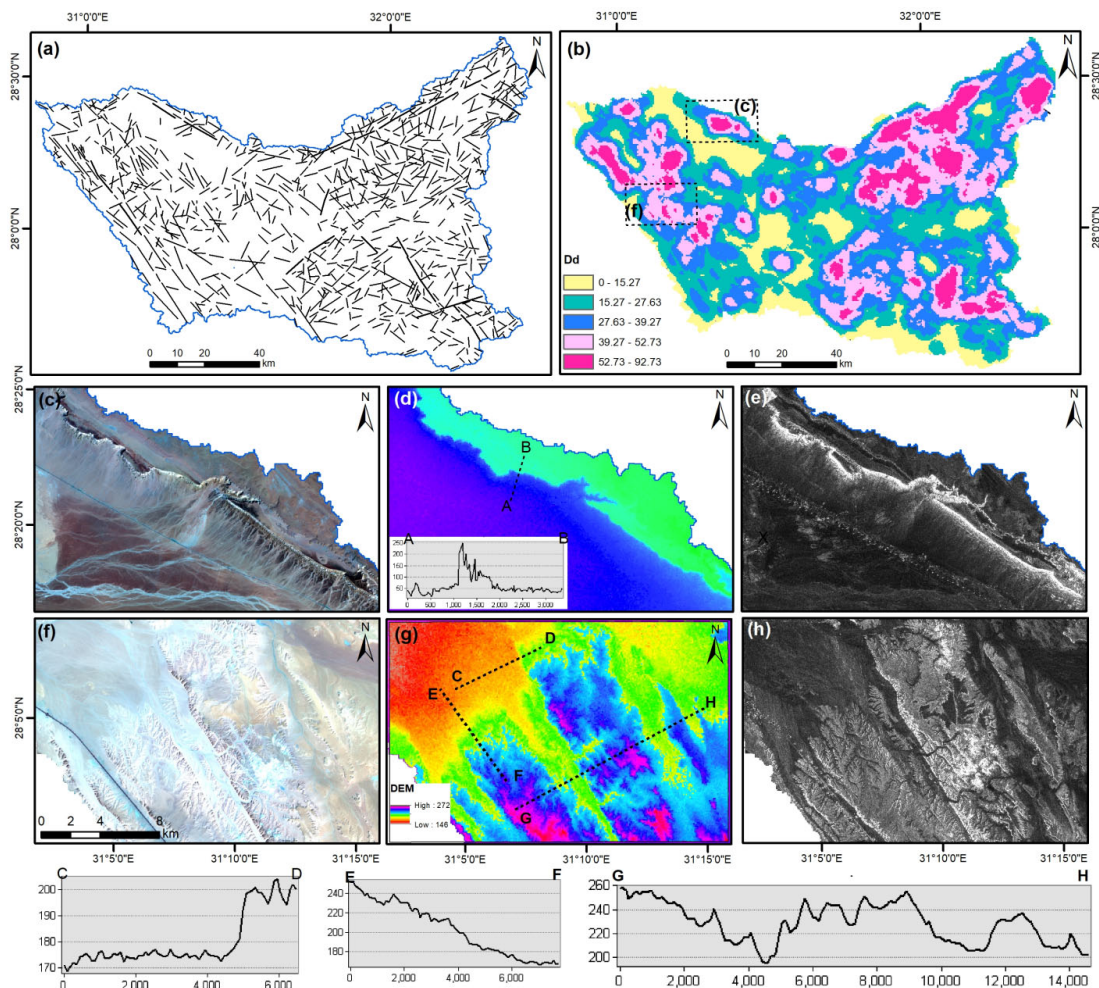


**Figure 5.** (a) Lineament map of W. El-Tarfa and (b) lineament density map; polygon labeled “c” is the same area in (c–e) and polygon labeled “f” corresponds to area in (g,h). (c) Landsat-8 band composite 7, 5, and 3 displays linear feature-like fault; (d) SRTM-DEM displays contrast in altitude; (e) ALOS/PALSAR displays the ridge in white tone; (f) Landsat-8 displays drainage masked by sand; (g) elevation classification of SRTM-DEM data overlain by topographic profiles C–D, E–F, and G–H reflecting structural features; and (h) ALOS/PALSAR image displays the drainage lines that are masked by sand in the area.

#### 4.4. Altitude

It is often difficult to prospect water resources in areas of high elevation as water flows from the up-streams of the mountains and links in down streams with low elevations and high recharge probability [17]. Correspondingly, low elevation areas probably harvest surface water during heavy storms that drain through stream networks. This has an inverse impact on the occurrence and infiltration of groundwater potential as water tends to accumulate and store in areas of lower elevations than areas of higher elevations [53,54]. The altitude of the studied basin ranges from 27 m to 1260 m, with the higher elevation areas to the east and the lower to the west. An altitude map based on SRTM DEM data categorized five groups based on holding water, viz., very high, high, moderate, low, and very low, given weights of 8, 7, 5, 4, and 2, respectively, and covering 25.45, 24.65, 19.27, 20.91, and 9.71% of the entire area, respectively (Figure 6a,b; Table 3).

#### 4.5. Slope

The slope has positive relationships to runoff and hence has an inverse influence on infiltration and recharge capacity. With the increase of the slope angle values, the high velocity of overland flow will increase [55,56]. With a decreasing slope angle, the infiltration increases; hence, more surface water would penetrate to the aquifers below [2,3,30]. Areas of flat terrain allow precipitated water to infiltrate and percolate, but the steep slope areas produce fast overland flow and runoff from the uplands and control the small amount of water for groundwater recharge. It can be observed that the slope degree map of Wadi El-Tarfa ranges from 0 to 57.35 degree and is classified into five classes based on their importance for infiltration and groundwater occurrences [53,57,58]. Therefore, the slope angle classes are classified based on groundwater infiltration capability to very high, high, moderate, low, and very low 0–3, 3–5, 5–10, 10–15, and 15–57.35, respectively (Figure 6c,d), covering 54.72, 26.48, 14.95, 2.68, and 1.18% of the area, respectively (Table 3).

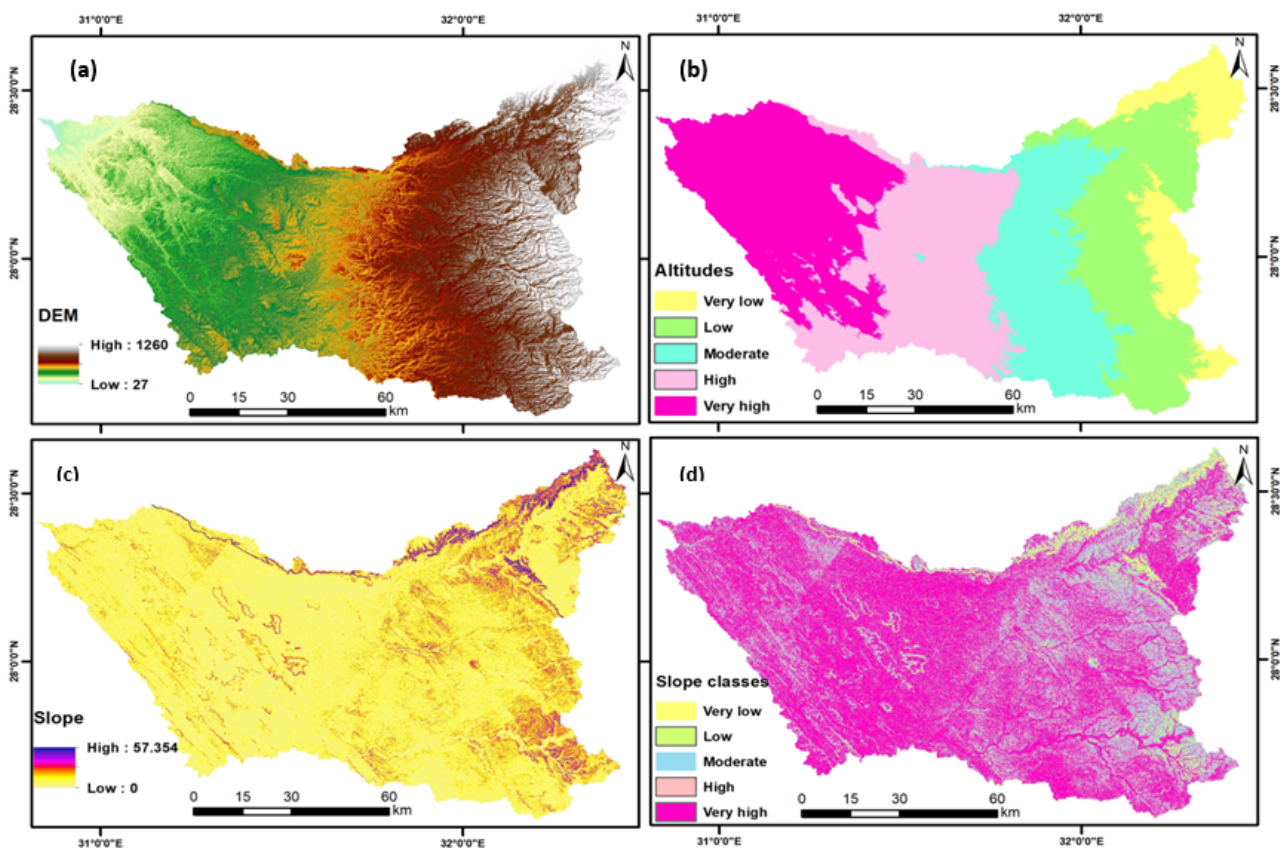
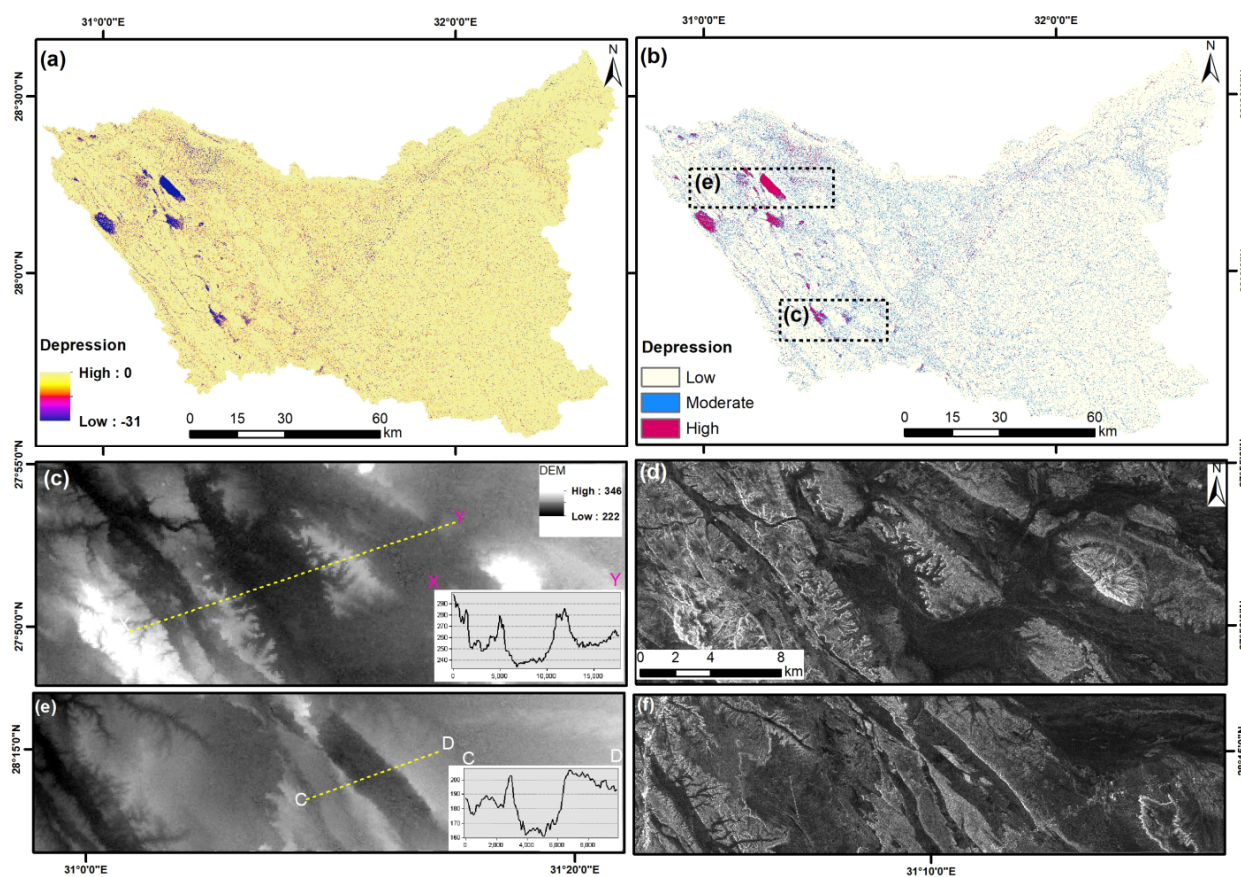


Figure 6. (a) DEM map of Wadi El-Tarfa; (b) reclassified DEM map; (c) slope degree; (d) slope classes.

#### 4.6. Depressions

Depressions that are low elevated areas that are surrounded by high relief collect, capture, and store precipitated water during the runoff of heavy storms in areas of arid/hyperarid climatic conditions. Areas that accumulate water can be inundated by water until it evaporates and infiltrates through the strata and into the aquifers underneath [2,7]. These depressions can be filled with precipitated water until the water elevation reaches a level at which the flow would pour out of the depression. These areas are promising for water resources as they inundate the low altitudes. This can be extracted from SRTM DEM (Figure 7a,b) using spatial analysis of Arc Map v. 10.5 (Esri, Redlands, CA, USA) by subtracting the original DEM from the filled-DEM in what is called “fill-difference” [2]. The depressions are validated using elevation profiles derived from SRTM DEM and ALOS/PALSAR data (Figure 7c–f). The resulting map is classified into three classes, which are  $-31$  to  $-2.64$  (high),  $-2.64$  to  $-0.72$  (moderate), and  $-0.72$  to  $0$  (low), based on the ability to collect and accumulate precipitated water that would infiltrate to the groundwater aquifers, and they cover 2.64%, 7.42%, and 89.94%, respectively, of the entire basin (Figure 7b; Table 3).



**Figure 7.** (a) Depression map and (b) depression classes map. (c) DEM depicted in (b) displays low elevated areas as shown in X-Y profile; (d) ALOS/PALSAR data for same area in “c” displays low elevated areas in dark tone; and (e) DEM displays depressions as indicated in profile C-D and marked in ALOS/PALSAR data in dark tone in (f).

#### 4.7. Surface Curvature

Land surface curvature represents an important factor related to accumulation and infiltration capacity. The land surface curvature layer is derived from the DEM and labeled into three classes: concave, convex, and flat (Figure 8a,b). Land surface curvature (radians/100 m) characterizes the areas that would capture water resources derived from the precipitation. Curved and flat areas more easily accumulate water and yield infiltration

capacity than convex areas. Water tends to accumulate in the concave and flat land surfaces; hence, the areas of high curvature values were given high weight values and vice versa [18]. The results of the curvature map range are from three classes, viz., low ( $-3.774$  to  $-0.0888$ ), moderate ( $0.0888$ – $0.1397$ ), and high ( $0.1397$ – $2.8339$ ), covering 25.84%, 27.11%, and 47.05% (Table 3), respectively, as curvature positively relates to water accumulation.

#### 4.8. Topographic Wetness Index (TWI)

The TWI refers to the size of flow accumulation at a certain point in the watershed and the tendency of water to flow downslope under the force of gravity [39,59], which accelerates water flow accumulation and can also describe the wetness conditions of a region [18,60]. Several studies have implemented the TWI in mapping potential areas of groundwater [18,19,61].

The TWI can be estimated by the following equation:

$$TWI = \ln (Ac/\tan S) \quad (5)$$

where  $Ac$  is the specific catchment area ( $m^2/m$ ) and  $S$  is the slope gradient (in degrees).

TWI values of the W. El-Tarfa basin ranged between 4.78 and 17.69 as displayed in Figure 8c,d. The TWI is classified into four sub-classes which are very high (11.31–17.69), high (9.84–11.31), moderate (8.07–9.48), and low (4.78–8.07) (Table 3). The TWI is positive to recharge potentials and GWPZs as high values of TWI were given higher weights and vice versa [18,27].

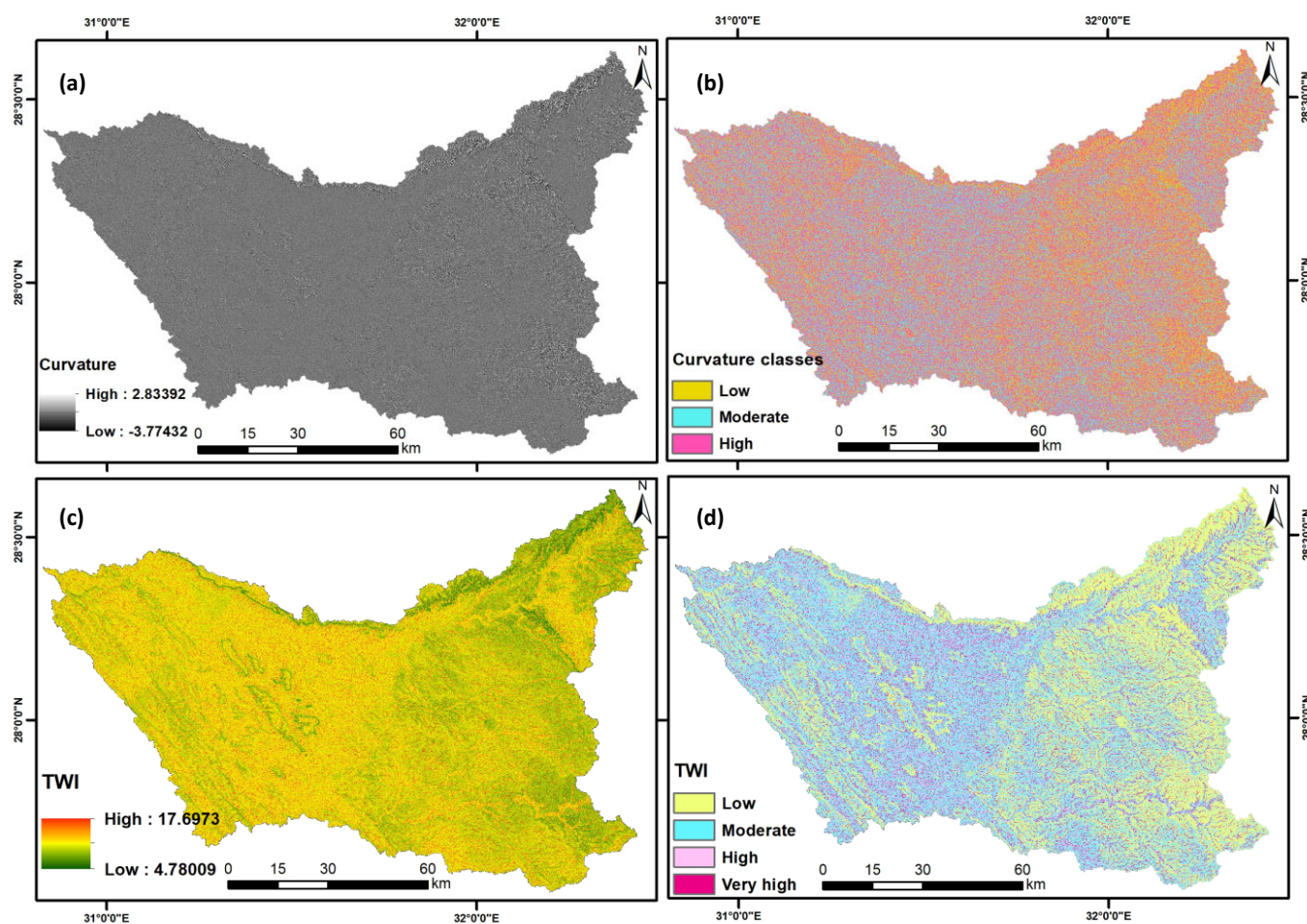
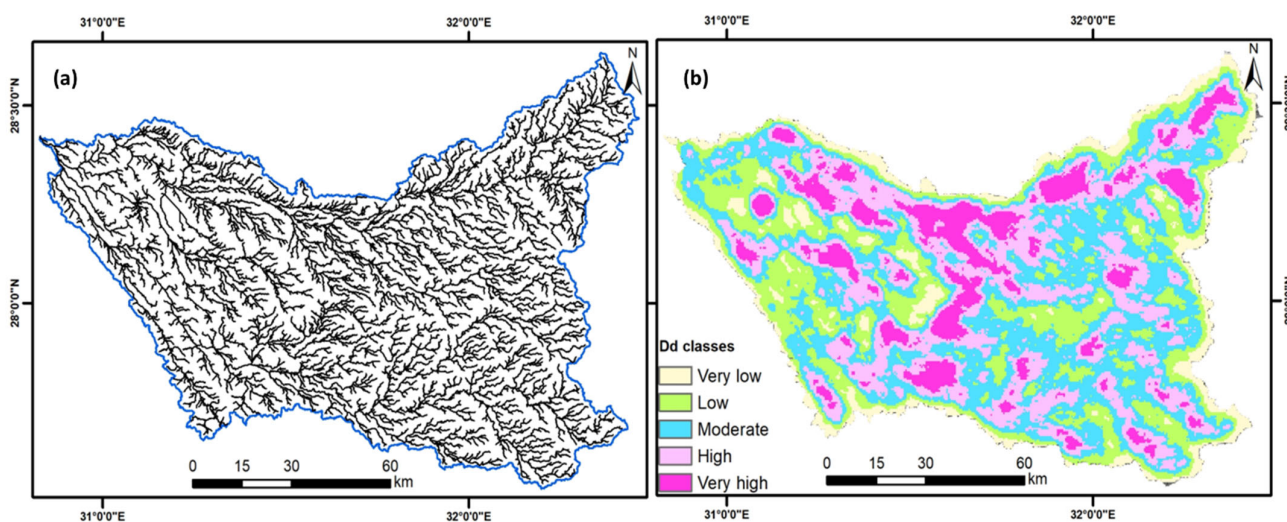


Figure 8. (a) Curvature derived from DEM; (b) curvature classes; (c) TWI; (d) TWI classes.

#### 4.9. Drainage Density

The drainage network density reflects surface-to-subsurface formation and is inversely related to the rate of permeability and recharge processes, as the high values of Dd yield surface runoff [7,18,32,35,62,63]. However, drainage networks that catch sizable quantities of precipitation would promote infiltration and recharging potentiality as a greater quantity of water results in more water recharging and infiltration. Hence, zones of high Dd are favorable zones for recharging groundwater, particularly in highly dissected land surfaces [2,3,64,65]. Thus, drainage density is estimated as the total length per unit area of the stream network,  $Dd = \Sigma Ls/A$ .

Based on the Dd map (Figure 9a), the high Dd values were given a high grade of 5 and discriminated into 5 classes: very low, low, moderate, high, and very high, based on holding, recharging, and controlling the groundwater availability and covering areas of 9.10, 22.35, 31.66, 25.39, and 11.51%, respectively (Figure 9a; Table 3). The zones with high Dd density promote more infiltration and GW recharge [64].



**Figure 9.** (a) Extracted drainage networks and (b) drainage density.

#### 4.10. Runoff Using Physical Characteristics of Catchments

Basin catchments that receive water from annual rainfall represent the main sources in arid/hyperarid regions that recharge the groundwater aquifers, and the harvested amount behind dams is utilized in agricultural activities. The quantitative morphometric characteristics of the catchments are calculated based on the SRTM DEM data [2,12,41] that control the runoff and infiltration capacity (Appendix A). The W. El-Tarfa watershed, covering about 10,605 km<sup>2</sup> with a perimeter of 962 km and a stream order of 7 (Figure 10a), is here subdivided into 26 sub-basins to estimate runoff potential (Figure 10b,c). In this basin, the extracted stream number is 4749 with a total length of about 10,597 km. The areas of the sub-basins range from 52 to 790 km<sup>2</sup>, and perimeter from 68 to 318 km. Based on the topographic data derived from the analysis of DEM, the computed twelve quantitative morphometric indices display variation from one sub-basin to another (Appendices A and B).

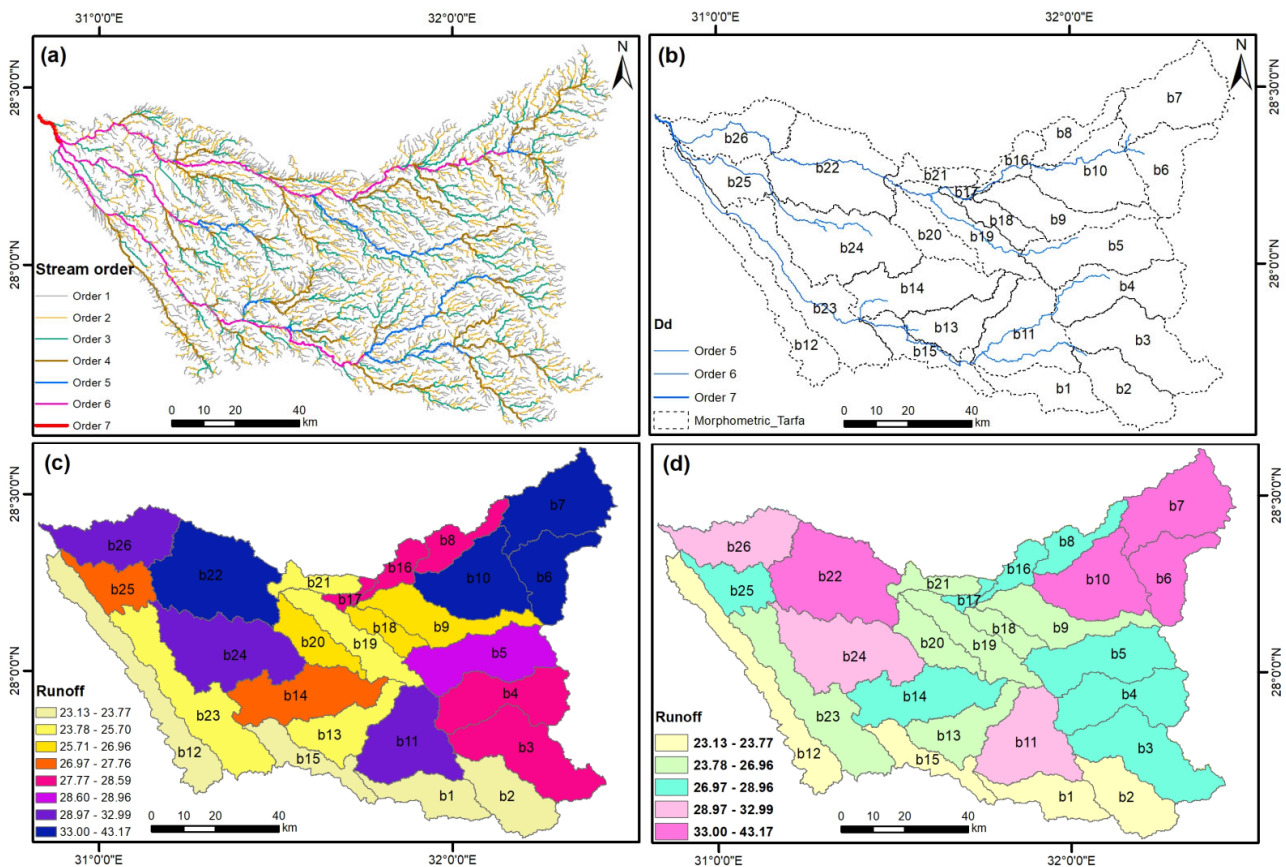


**Figure 10.** (a) Stream order for Wadi El-Tarfa basin; (b) sub-basins of Wadi El-Tarfa basin, the detached lines represent the division of sub-basins; (c) values of runoff for sub-basins; and (d) classes of runoff values for sub-basins.

The bifurcation ratio ( $R_b$ ) and the length of overland flow ( $L_g$ ) have positive relation to infiltration and a negative relation to runoff [2,12]. The  $R_b$  of the studied sub-basins ranges from 3.41 to 6.14 with an average of 3.97 (Appendix A). The lowest values of  $R_b$  imply the highest water flow and a low infiltration capacity [12,41]. The  $L_g$  values extend between 0.26 and 0.33 with an average of 0.50. In contrast to  $R_b$  and  $L_g$ , there are 10 other factors positively related to runoff. Three of these factors characterizing the geometric shape (either circular or elongated) are the elongation ratio ( $R_e$ ), circularity ratio ( $R_c$ ), and form factor ( $R_f$ ). The computed  $R_e$  [66] values range from 0.31 to 1.22 with an average of 0.65 (elongated). The highest values were recorded in #b6; however, the lowest was in #b12. The  $R_c$  ranges from 0.07 (#12) to 0.26 (sub-basins #b10 and b11) with an average of 0.14, referring to an elongated rather than a circular shape [12]. In addition to  $R_e$  and  $R_c$ , the  $R_f$  [67] ranges from 0.08 (sub-basin #b12) to 1.16 (sub-basin #6) with an average of 0.34, implying an elongated rather than a circular form. In addition to the shape of catchments, the drainage texture ( $R_t$ ), stream frequency ( $F_s$ ), and infiltration factor ( $I_f$ ) are of crucial importance in understanding the distribution of streams with the basin and hence in estimating the runoff potential [12,41]. The  $R_t$  describe the relationships of stream numbers and the perimeter ( $p$ ) of a selected sub-basin [64]; thus, the  $R_t$  ranges from 1.04 to 5.56 with an average of 4.93 that implies a medium to coarse texture [12]. Additionally, the  $F_s$  [67] ranges from 1.21 (#b2) to 1.57 (#b25) with an average of 0.45, reflecting a low to medium relief [12]. The calculated  $I_f$  [68] characterizes the infiltration properties that directly influence runoff and ranges between 1.84 (#b2) and 2.89 (#b22) with an average of 0.45 (Appendix A).

The basin relief ( $B_h$ ) [44,69] of W. El-Tarfa, which characterizes the contrast between the highest and lowest elevation points, ranges from 0.16 to 0.67. Two other factors derived from  $B_h$  are the relief ratio ( $R_h$ ) and ruggedness number ( $R_n$ ), which contribute to runoff

capabilities [2,12,41]. The  $Rh$  reflects the influence of the runoff by the slope gradient, and it extends between 0 and 0.02. The  $Rn$  values extends between 0.26 (#b25) and 1.06 (#b7).

The aforementioned factors are normalized using linear equations [70], Equations (5) and (6), to estimate the runoff capability. All the parameters are normalized using Equation (5), but the  $Rb$  and the  $Lg$  are normalized using Equation (6) (Appendices A and B) as follows:

$$\text{Hazard degree} = \frac{4(X - X_{min})}{(X_{max} - X_{min})} + 1 \quad (6)$$

$$\text{Hazard degree} = \frac{4(X - X_{max})}{(X_{min} - X_{max})} + 1 \quad (7)$$

where  $X$  represents the value of parameters to be calculated for the flood potentials for each sub-basin. It is worth noting that the potential runoff weights (Figure 10d; Appendix B) range from 23.13 (sub-basin#1) to 43.17 (sub-basin#6).

#### 4.11. Rainfall

During heavy storms, recharge often occurs, and the excessive amount of rainfall within a very short period of time causes a flash flood [71]. The intensity and span of rainfall control the amount of infiltration and runoff. Therefore, rainfall factor is extremely important in studying the water accumulation and determining groundwater recharging as it represents the source of water in arid regions [2,18]. Rainfall has a positive relationship to groundwater recharging as the higher the annual rainfall, the higher the groundwater recharge potentials [72].

Wadi El-Tarfa often receives heavy seasonal rainfall which is driven by elevation as its upper stream (1260 m a.s.l) is a part of the elevated plateau of G. El-Galala El-Qibliya. The Wadi El-Tarfa basin experienced heavy rainfalls during 29 December 2010, 17 to 18 January 2010, 8 to 9 March 2014, and 2015 (Figure 11a–d). The spatial distributions of rainfall intensity are different from one storm to another, as illustrated in Figure 11. Such storms replenish the magnitude of groundwater level by charging, particularly the shallow aquifers, after inundating streams to add groundwater resources. Average daily precipitated data were collected from the TRMM satellite during the period of 1 January 1998 to 30 November 2015 and were interpolated using the inverse distance weighted (IDW) method in GIS to display the precipitation intensity in W. El-Tarfa (Figure 11a). The average rainfall map with a range from 0.012 to 0.087 mm/daily (Figure 11e,f) is classified into three classes, viz., low, moderate, and high (Figure 11b), covering 70.31, 18.08, and 11.61% of the area (Table 3). The high value of precipitation assigned a high weight and high recharge potentials to groundwater. Based on the spatial distribution, the average rainfall intensity is higher in the northeast (W. Ragala and W. Abu Ratam) and southwest portions of the area (W. El-Dahasa) (Figure 11a,b).

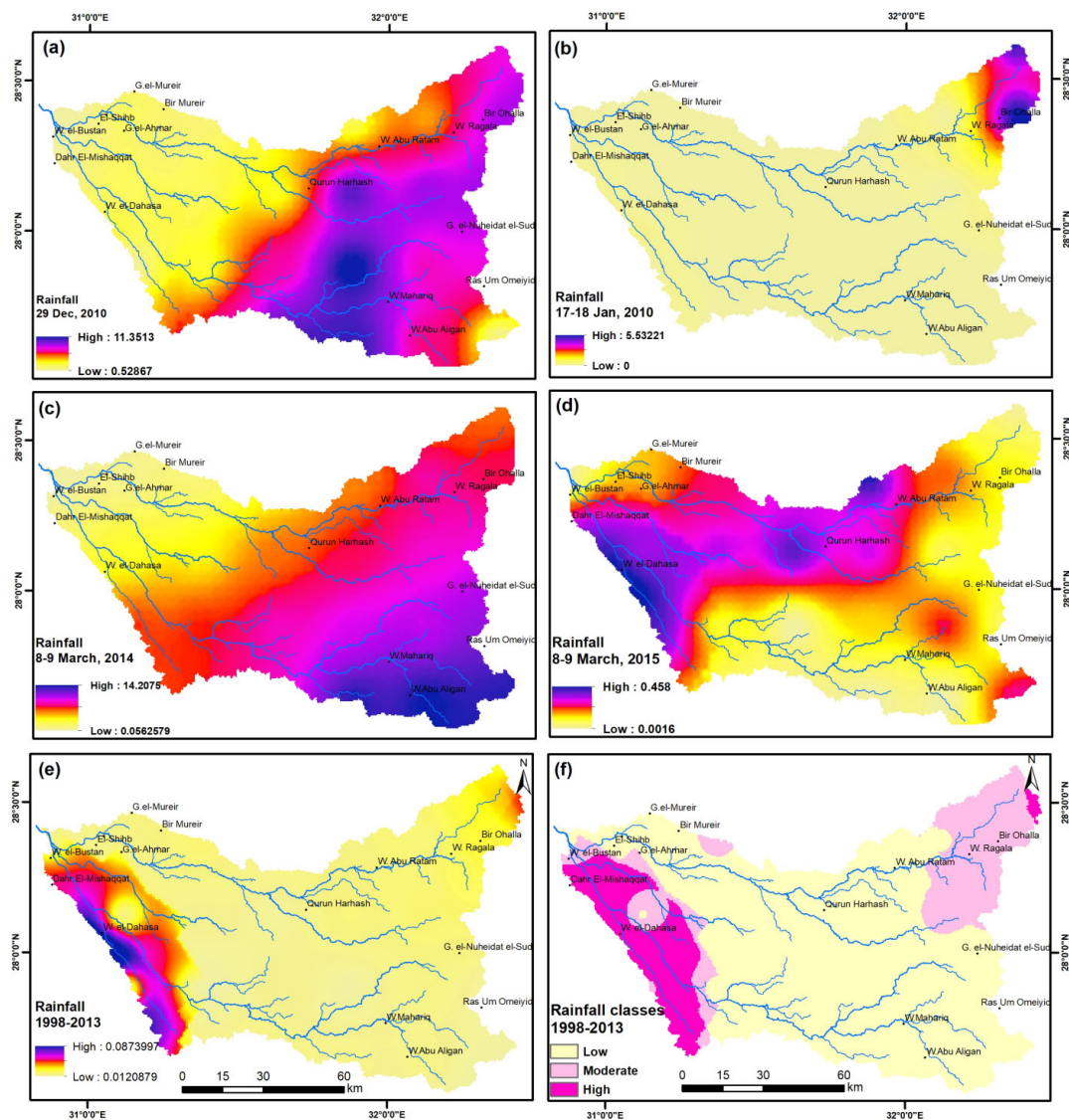


**Figure 11.** Rainfall data derived from TRMM in mm/day: (a) rainfall storm on 29 December 2010; (b) rainfall storm on 17 to 18 January 2010; (c) rainfall storm on 8 to 9 March 2014; (d) rainfall storm on 8 to 9 March 2015; and (e,f) average rainfall (years 1998–2015) in Wadi El-Tarfa.

### 5. Groundwater Prospective Zones (GWPZs)

The output GWPZs map was created by combining 11 input evidential maps describing the geology, hydrology, topographic, and climatic conditions of Wadi El-Tarfa, such as lithology, radar intensity, lineaments, elevation, slope, curvature, depressions, TWI, drainage density, runoff, and rainfall.

Based on the variations on the input maps, eleven thematic maps were prepared to increase the value and prediction of the output GWPZs map (Figure 12). The input layers and sub-classes were normalized based on the APH method after assigning weights depending on Saaty's scale as displayed in Table 3. Once these layers were prepared and given weighting coefficients, they were combined through the multi-criteria GIS-based weighted linear combination method. The GWPZs were obtained using the process of the thematic layers, which allows the accumulated weights of each pixel to be calculated after assigning weights for each layer and sub-class, which can be calculated using Equation (3).

The GWPZs map (Figure 12) is grouped into five zones, which are very high, high, moderate, low, and very low, covering 10.32%, 24.98%, 30.47%, 24.02%, and 10.20% of the entire basin area, respectively. Based on the GWPZs map, zones of very high and high occupy the most promising areas.

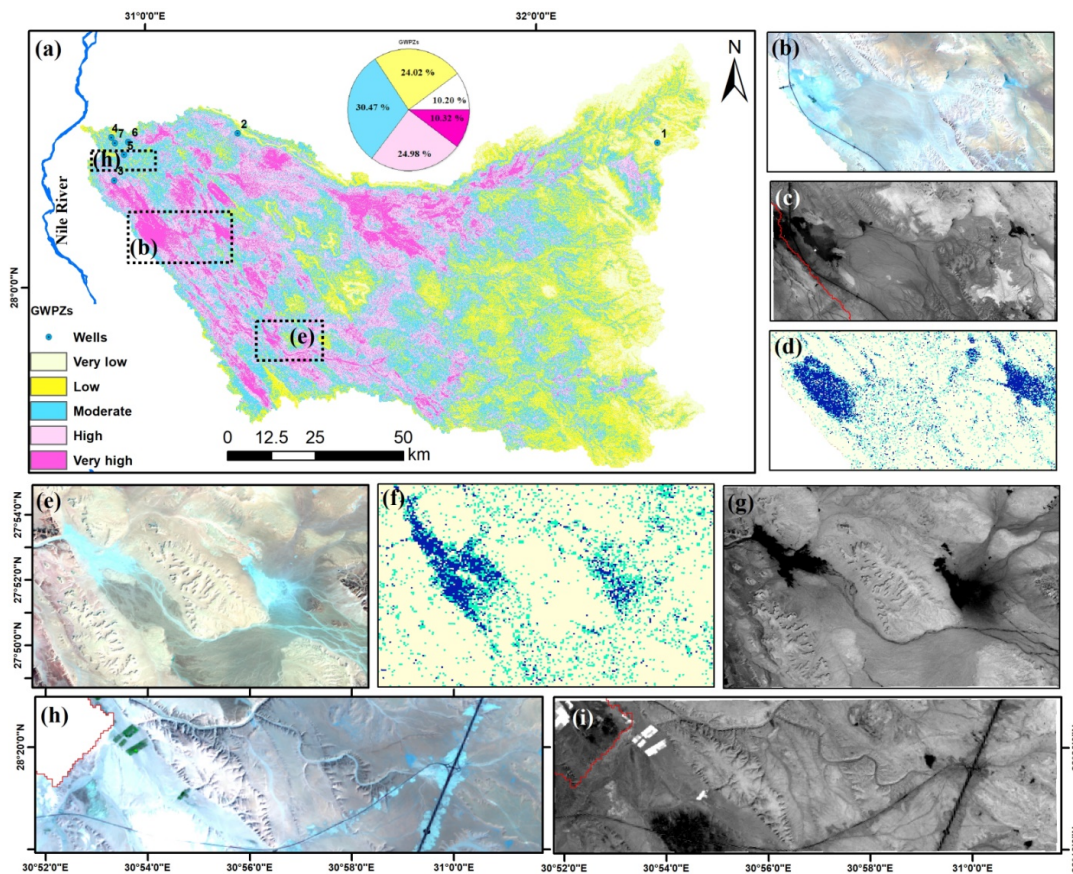


**Figure 12.** (a) GWPZs overlain by well data (#1 and 2 [42], #3–7 [73]; (b,e,h) subsets of OLI that were acquired on 15 March 2014 after storm on 8–9 March 2014; (c,g,i) NDVI of OLI subsets; and (d,f) extracted depressions derived from SRTM DEM.

The GWPZs were verified with the observations of the Landsat-8 data 7, 5, and 3 in R, G, and B that were acquired on 15 March 2014, after the storm of 8 to 9 March 2014. This image revealed the presence of a surface water signature in cyan. Based on water bodies having strong absorption in the visible/infrared wavelengths range, the water bodies would appear in dark signatures of NDVI. Its values vary from  $-1$  to  $1$ ; the higher values of NDVI reflect dense greenery and the low values less than zero would reveal water bodies [46] (Figure 12e,f,i). Therefore, water accumulated in lowlands as depicted by NDVI, OLI, and the extracted depressions. The concordance between NDVI, OLI, and the extracted depressions shows valuable results. The well data (#1, 2) derived from Conoco [42] and #3–7 [73] are consistent with moderate to high groundwater potential zones, except #1, which fits the low to very low zones (Figure 12a). The validation process confirms that the GWPZs map prepared from GIS and AHP techniques is effective, represents the technique, and can be used precisely and efficiently to determine the GWPZs.

## 6. Discussion

Wadi El-Tarfa, east of Egypt's Nile River, covers  $\sim 10,605$  km<sup>2</sup> and is recognized as a major target for groundwater exploitation, as it represents one of the most promising areas for agriculture development. In this study, a groundwater potential map using the AHP-weighted overlay model (Figure 12) was created by combining eleven input evidential maps describing the geology, hydrology, topography, and climatic conditions of Wadi El-Tarfa. Based on combining these data through GIS using Equation (3), the potential area of GWPZs covers 10.32% of the study area, representing the low elevation, high rainfall, and high lineament and drainage density in areas of low slope and rich in alluvial deposits. Combining these data through GIS-based AHP-overlay approaches [4,5,17,18,20,31,32] allowed the prediction

of the prospective sectors for GWPZs with the AHP technique, which depends on extracting ratio rates from the paired comparison and represents an easy solution for complex decision analysis that successfully revealed potential areas of groundwater.

Topographic parameters, e.g., altitude, depressions, slope, and curvature, contributed to predicting the possible locations of groundwater. The high altitudes of up to 1260 m (a.s.l) and geomorphic features of Wadi El-Tarfa promote rainfall as precipitation is driven by topography; it was shaped by the uplift which is caused due to subsurface convection processes in the areas northwest of the Gulf of Suez [74]. Although areas of high altitudes received high precipitation and runoff, areas of low altitudes in the downstream (25.45%) allow for water infiltration and accumulation [2,32,53,54,75] as most of these areas are classified as having high to very high potentiality (Figure 12a). Characterizing certain low elevations that are surrounded by high relief, called “depressions”, they are highly predicted areas for harvesting surface water accumulation during heavy storms as the water of drainage networks tends to accumulate at lower elevations of the downstream of W. El-Tarfa versus higher elevations [53,54]. Areas of depressions have signatures of surface water resources as depicted by Landsat-8 and NDVI (Figure 12e–g). The variation in elevation generates slope, which has a positive relationship to runoff and hence has an inverse influence on infiltration and recharge capacity [38,55,56]. Thus, the areas of flat to gentle slope [76] that totally cover ~54% of the basin are assigned the very high potentiality and contributed to generating the GWPZs map because of high infiltration and low runoff (Figure 12). Moreover, the curvature factor, which identifies the change in slope gradient, contributed to the output map [77]. Thus, curvatures and flat surfaces allow for collecting water and promote more infiltration capability than convex areas. Thus, high curvature values were assigned high weight values that covered ~47% of the entire basin.

Lineaments include faults and fracture zones caused by the response to tectonic movements and the deformation of rocks [28] and reflect a crustal weakness zone with prominent relationships to the movement, occurrence, and storing of groundwater [34]. These zones induce permeability and secondary porosity [78,79] as they have a valuable task in controlling the recharge potentiality, particularly in the hard Eocene rocks of the basin. It is worth noting that these zones are mostly coincident with drainage lines and areas of fine deposits (Figure 5). Hence, areas with high lineament density facilitated water infiltration and penetration [75], and therefore water accumulation and the prospective for groundwater potential and vice versa [2,29,53,57]; it was depicted in the GWPZs of the study area that the majority of areas of high to very high prospective zones are consistent with high lineament density. More than 30% of the basin is characterized by high lineament density, which favors the circulation of the precipitated water into the strata below, particularly the northeastern and southwestern parts.

Classifying the backscatter intensity of ALOS/PALSAR data also contributed to revealing the geomorphic features and surface roughness along with geological structures. This is because it allowed for identification of the fluvial deposits that accumulated on the streams and low elevation areas and appeared as a dark signature, covering about 27% of the basin (Figures 4, 5h and 7d,f), mostly the downstream areas along the main drainages and along faults which are difficult to recognize in OLI images (Figure 4). Sand and gravel accumulation zones would be regarded as prime water accumulation zones [2,80] as revealed by the high to very high GWPZs that are consistent with the dark signature of the radar data. These exposed wadi deposits, which are highly permeable, would catch and capture surface water flow along the main streams and downstream areas and prove the existence of groundwater [73,81].

The hydrologic factors (TWI, Dd, and runoff) clearly contributed to preparing the GWPZs map. TWI has a positive relationship with recharge potentials and GWPZs, with greater TWI values resulting in higher weights [27]. This is because the TWI factor identifies the moisture characteristics [8,82]. Moreover, understanding the drainage networks allows for the GWPZs and geomorphic characteristics to be revealed as the areas of the dendritic pattern are developed in regions underlain by homogeneous rocks [78] as the plateau of the studied basin is built up of limestone. The drainage networks that catch sizable

quantities of precipitation would promote infiltration and recharging potentiality as a greater quantity of water results in more water recharging and infiltration in the basin as the majority of the basin is gentle slope. Hence, zones of high Dd that cover 11.51% of the area contribute to recharging groundwater, particularly in gentle slope and highly dissected land surfaces [2,3,64,65] and at the northern part of the present study (Figure 9b). This clearly contributed to producing the output map, as the northern part of high Dd displays a high to very high potentiality (Figure 12a). Furthermore, computing morphometric parameters of 26 sub-basins showed that the runoff is inversely related to infiltration (Appendices A and B). This is because these parameters characterized the morphometric, geometric, and relief characteristics of the basin that correlated to infiltration capabilities [2].

Climatic conditions such as rainfall are also of high importance in predicting the GWPZs [83]. During heavy rainfall, the W. El-Tarfa basin harvests a sizable amount of water that recharges the shallow aquifers that would help in sustainable development. During the 1994 flood event, the W. El-Tarfa groundwater shallow aquifer recharged by  $15.8 \times 10$  m as the detected transmission losses ranged from 21 to 31% [84]. W. El-Tarfa received a high amount of precipitation during storms on 29 December 2010; 17 to 18 January 2010; and 8–9 March 2014, for example. The signature of the accumulated water was realized by Landsat-8 and NDVI data that were acquired after the storm of 8–9 March 2014 as water bodies have strong absorption in the visible/infrared EM regions and appear in dark signatures of NDVI, which extends from  $-1$  to  $1$ . These areas of water signatures are consistent with areas of moderate to very high groundwater potentiality (Figure 12a).

## 7. Conclusions

Groundwater is a vital source of water for sustainable development, particularly in arid and hyperarid regions. The fusion of remote sensing data including SRTM, ALOS/PALSAR, TRMM, and Landsat-8 OLI data through GIS approaches successfully allowed reconnaissance information for water resources to be revealed, assessed, and monitored in the present study. Wadi El-Tarfa, which covers a  $\sim 10,605$  km<sup>2</sup> area, was tested to reveal promising zones of groundwater potentiality using multi-criteria. Eleven predictive GIS maps representing geologic, geomorphic, climatic, and hydrologic conditions, e.g., geology, altitude, slope, drainage density, topographic wetness index (TWI), curvature, and depressions, were considered. In addition, morphometric characteristics, radar intensity, and rainfall obtained from optical and radar satellite images were normalized and integrated using AHP-weighted overlay techniques. The fusion was done using the eleven evidential maps through the GIS-based overlay approach to demarcate promising areas of groundwater. The obtained GWPZs map was then grouped into five classes, i.e., very high, high, moderate, low, and very low potentiality. These areas cover 10.32%, 24.98%, 30.47%, 24.02%, and 10.20%, respectively, of the study area. Overall, probing areas of GWPZs is helpful to decision-makers of the study area, who are considering sustainability.

**Author Contributions:** Conceptualization, M.A.; methodology, M.A.; software, M.A.; validation, M.A., F.A. and N.A.-A.; formal analysis, M.A.; investigation, M.A., F.A. and N.A.-A.; resources, M.A. and N.A.-A.; data curation, M.A.; writing—original draft preparation, M.A., A.M., N.A.-A., F.A. and F.E.-B.; writing—review and editing, M.A., A.M., N.A.-A. and F.E.-B. All authors have read and agreed to the published version of the manuscript.

**Funding:** This research received no external funding.

**Data Availability Statement:** Satellite images were acquired from U.S. Geological Survey (USGS) and Earth explorer websites. Data are available upon request.

**Acknowledgments:** Nasir Al-Arifi extends his grateful to the Deanship of Scientific Research, King Saud University for funding through the Vice Deanship of Scientific Research Chairs.

**Conflicts of Interest:** The authors declare no conflict of interest.

## Appendix A

Table A1. Morphometric parameters of Wadi El-Tarfa.

Basin#	U-Order	Nu	Lu	Area (km <sup>2</sup> )	P (km)	Lb (km)	Rb	Re	Rf	Rc	Rt	Fs	Dd	Lg	If	Bh (km)	Rh	Rn	Cm	W
1	5	403	469.10	301.93	146.68	41.04	4.30	0.48	0.18	0.18	2.75	1.33	1.55	0.32	2.07	0.26	0.01	0.40	0.64	14.19
2	5	469	588.46	387.68	141.07	35.89	4.54	0.62	0.30	0.24	3.32	1.21	1.52	0.33	1.84	0.27	0.01	0.41	0.66	16.71
3	5	812	952.20	599.45	191.78	44.01	5.09	0.63	0.31	0.20	4.23	1.35	1.59	0.31	2.15	0.38	0.01	0.61	0.63	19.25
4	6	624	775.99	492.72	173.37	38.91	3.79	0.64	0.33	0.21	3.60	1.27	1.57	0.32	1.99	0.38	0.01	0.60	0.63	19.02
5	6	681	832.26	533.35	177.33	42.77	3.74	0.61	0.29	0.21	3.84	1.28	1.56	0.32	1.99	0.41	0.01	0.64	0.64	18.72
6	5	526	642.08	361.41	144.44	17.65	4.50	1.22	1.16	0.22	3.64	1.46	1.78	0.28	2.59	0.40	0.02	0.71	0.56	32.26
7	6	775	886.75	559.80	181.24	35.71	3.80	0.75	0.44	0.21	4.28	1.38	1.58	0.32	2.19	0.67	0.02	1.06	0.63	22.63
8	5	270	318.49	198.50	131.28	34.82	4.05	0.46	0.16	0.14	2.06	1.36	1.60	0.31	2.18	0.48	0.01	0.77	0.62	11.24
9	5	495	642.66	390.41	193.40	53.41	4.58	0.42	0.14	0.13	2.56	1.27	1.65	0.30	2.09	0.52	0.01	0.86	0.61	15.81
10	6	717	858.52	537.91	160.51	27.04	3.64	0.97	0.74	0.26	4.47	1.33	1.60	0.31	2.13	0.40	0.01	0.64	0.63	28.27
11	6	746	918.95	567.57	165.66	33.29	3.84	0.81	0.51	0.26	4.50	1.31	1.62	0.31	2.13	0.23	0.01	0.38	0.62	33.98
12	5	840	963.70	559.43	318.50	84.96	5.18	0.31	0.08	0.07	2.64	1.50	1.72	0.29	2.59	0.28	0.00	0.49	0.58	13.23
13	6	447	556.70	344.05	167.99	36.56	3.49	0.57	0.26	0.15	2.66	1.30	1.62	0.31	2.10	0.27	0.01	0.44	0.62	18.32
14	5	752	952.81	535.75	213.08	43.26	5.16	0.60	0.29	0.15	3.53	1.40	1.78	0.28	2.50	0.25	0.01	0.45	0.56	18.53
15	6	362	429.79	256.57	183.20	44.08	3.41	0.41	0.13	0.10	1.98	1.41	1.68	0.30	2.36	0.19	0.00	0.32	0.60	10.06
16	5	197	241.33	139.73	111.35	28.67	3.69	0.47	0.17	0.14	1.77	1.41	1.73	0.29	2.43	0.32	0.01	0.55	0.58	9.30
17	4	72	98.61	52.07	68.98	16.18	3.89	0.50	0.20	0.14	1.04	1.38	1.89	0.26	2.62	0.20	0.01	0.38	0.53	6.40
18	5	188	265.06	149.97	97.85	26.00	3.66	0.53	0.22	0.20	1.92	1.25	1.77	0.28	2.22	0.25	0.01	0.44	0.57	8.78
19	5	452	615.83	347.69	185.91	49.38	4.35	0.43	0.14	0.13	2.43	1.30	1.77	0.28	2.30	0.31	0.01	0.55	0.56	12.83
20	5	364	443.10	251.98	142.73	36.76	4.27	0.49	0.19	0.16	2.55	1.44	1.76	0.28	2.54	0.19	0.01	0.34	0.57	11.04
21	4	199	264.88	142.94	110.19	26.42	6.14	0.51	0.20	0.15	1.81	1.39	1.85	0.27	2.58	0.25	0.01	0.46	0.54	9.29
22	6	1202	1503.34	790.38	216.23	39.33	3.97	0.81	0.51	0.21	5.56	1.52	1.90	0.26	2.89	0.26	0.01	0.50	0.53	28.40
23	6	1030	1109.50	679.14	285.34	65.66	4.01	0.45	0.16	0.10	3.61	1.52	1.63	0.31	2.48	0.20	0.00	0.33	0.61	16.23
24	6	1096	1244.68	715.30	225.40	48.45	3.93	0.62	0.30	0.18	4.86	1.53	1.74	0.29	2.67	0.25	0.01	0.43	0.57	26.58
25	5	411	422.21	262.08	140.21	30.98	4.28	0.59	0.27	0.17	2.93	1.57	1.61	0.31	2.53	0.16	0.01	0.26	0.62	19.43
26	5	683	781.07	453.86	187.74	39.69	4.84	0.61	0.29	0.16	3.64	1.50	1.72	0.29	2.59	0.32	0.01	0.55	0.58	19.15
El-Tarfa	7	4749	10,597.40	10,611.68	962.35	177.89	3.97	0.65	0.34	0.14	4.93	0.45	1.00	0.50	0.45	1.24	0.01	1.23	1.00	123.81

## Appendix B

**Table A2.** Calculating runoff of Wadi El-Tarfa.

Basin #	Rt	Rb	Lg	Re	Rf	Rc	Fs	If	Bh	Rh	Rn	Runoff Weight
1	2.51	3.69	1.46	1.73	1.38	2.93	2.39	1.90	1.76	1.67	1.71	23.13
2	3.02	3.34	1.00	2.35	1.83	4.58	1.00	1.00	1.83	1.91	1.73	23.59
3	3.83	2.54	1.88	2.39	1.86	3.62	2.62	2.19	2.72	2.15	2.72	28.52
4	3.26	4.43	1.72	2.46	1.92	3.64	1.63	1.60	2.74	2.40	2.71	28.51
5	3.48	4.50	1.54	2.31	1.79	3.82	1.75	1.59	2.95	2.34	2.89	28.96
6	3.30	3.41	3.88	5.00	5.00	3.92	3.74	3.84	2.85	5.00	3.23	43.17
7	3.86	4.43	1.83	2.92	2.34	3.84	2.95	2.35	5.00	4.23	5.00	38.75
8	1.90	4.06	2.07	1.63	1.32	2.17	2.68	2.31	3.48	3.19	3.52	28.33
9	2.34	3.28	2.54	1.46	1.22	1.84	1.65	1.95	3.82	2.38	3.98	26.46
10	4.03	4.65	1.97	3.90	3.43	5.00	2.37	2.10	2.85	3.39	2.87	36.56
11	4.06	4.36	2.24	3.19	2.61	4.94	2.17	2.10	1.56	1.81	1.58	30.62
12	2.41	2.41	3.35	1.00	1.00	0.36	4.26	3.84	1.95	1.06	2.13	23.77
13	2.43	4.87	2.23	2.15	1.66	2.37	2.00	2.01	1.86	1.90	1.89	25.37
14	3.20	2.43	3.90	2.29	1.77	2.26	3.16	3.50	1.72	1.58	1.95	27.76
15	1.83	5.00	2.86	1.43	1.20	1.00	3.24	3.00	1.22	1.26	1.29	23.33
16	1.64	4.59	3.40	1.67	1.34	2.10	3.23	3.27	2.24	2.66	2.45	28.59
17	1.00	4.29	4.93	1.84	1.45	2.00	2.93	3.96	1.31	2.92	1.60	28.23
18	1.78	4.63	3.80	1.96	1.53	3.42	1.49	2.44	1.68	2.34	1.89	26.96
19	2.23	3.61	3.83	1.50	1.24	1.73	2.01	2.77	2.18	1.67	2.45	25.22
20	2.33	3.74	3.71	1.77	1.40	2.43	3.62	3.67	1.24	1.45	1.39	26.75
21	1.68	1.00	4.58	1.87	1.47	2.25	3.04	3.82	1.68	2.31	2.00	25.7
22	5.00	4.17	5.00	3.19	2.60	3.80	4.47	5.00	1.79	1.74	2.18	38.94
23	3.27	4.12	2.40	1.59	1.30	1.21	4.42	3.43	1.30	1.00	1.33	25.37
24	4.38	4.24	3.53	2.37	1.84	2.94	4.60	4.14	1.68	1.42	1.85	32.99
25	2.67	3.72	2.14	2.22	1.72	2.72	5.00	3.61	1.00	1.45	1.00	27.25
26	3.30	2.90	3.34	2.29	1.78	2.58	4.29	3.85	2.25	2.03	2.45	31.06

Abbreviations: U—stream order; Nu—sum of streams; Lu—sum of stream lengths; P—perimeter; Lb—basin length; Rb—mean bifurcation ratio; Re—elongation ratio; Rf—form factor; Rc—circularity ratio; Rt—drainage texture; Fs—stream frequency; Dd—drainage density; Lg—length of overland flow; If—infiltration number; Bh—basin relief; Rh—relief ratio; Rn—ruggedness no.; Cm—maintenance coefficient; w—width.

## References

1. El-Baz, F. Sand accumulation and groundwater in the eastern Sahara. *Episodes* **1998**, *21*, 147–151. [\[CrossRef\]](#)
2. Zhu, Q.; Abdelkareem, M. Mapping Groundwater Potential Zones Using a Knowledge-Driven Approach and GIS Analysis. *Water* **2021**, *13*, 579. [\[CrossRef\]](#)
3. Abdelkareem, M.; El-Baz, F.; Askalany, M.; Akawy, A.; Ghoneim, E. Groundwater prospect map of Egypt's Qena Valley using data fusion. *Int. J. Image Data Fusion* **2012**, *3*, 169–189. [\[CrossRef\]](#)
4. Arulbalaji, P.; Padmalal, D.; Sreelash, K. GIS and AHP techniques Based Delineation of Groundwater Potential Zones: A case study from southern Western Ghats, India. *Sci. Rep.* **2019**, *9*, 2082. [\[CrossRef\]](#)
5. Abdelkareem, M.; Abdalla, F. Revealing potential areas of water resources using integrated remote-sensing data and GIS-based analytical hierarchy process. *Geocarto Int.* **2021**, 1–25. [\[CrossRef\]](#)
6. Abdelkareem, M.; El-Baz, F. Analyses of optical images and radar data reveal structural features and predict groundwater accumulations in the central Eastern Desert of Egypt. *Arab. J. Geosci.* **2014**, *8*, 2653–2666. [\[CrossRef\]](#)
7. Abdelkareem, M.; Al-Arifi, N. The use of remotely sensed data to reveal geologic, structural, and hydrologic features and predict potential areas of water resources in arid regions. *Arab. J. Geosci.* **2021**, *14*, 704. [\[CrossRef\]](#)
8. Yariyan, P.; Avand, M.; Omidvar, E.; Pham, Q.B.; Linh, N.T.T.; Tiefenbacher, J.P. Optimization of statistical and machine learning hybrid models for groundwater potential mapping. *Geocarto Int.* **2020**, *11*, 2282–2314. [\[CrossRef\]](#)

9. Scheuer, S.; Haase, D.; Volk, M. Integrative assessment of climate change for fast-growing urban areas: Measurement and recommendations for future research. *PLoS ONE* **2017**, *12*, e0189451. [[CrossRef](#)]
10. Ullah, K.; Zhang, J. GIS-based flood hazard mapping using relative frequency ratio method: A case study of Panjkora River Basin, eastern Hindu Kush, Pakistan. *PLoS ONE* **2020**, *15*, e0229153. [[CrossRef](#)]
11. Zhang, D.-W.; Quan, J.; Zhang, H.-B.; Wang, F.; Wang, H.; He, X.-Y. Flash flood hazard mapping: A pilot case study in Xiapu River Basin, China. *Water Sci. Eng.* **2015**, *8*, 195–204. [[CrossRef](#)]
12. Abdelkareem, M. Targeting flash flood potential areas using remotely sensed data and GIS techniques. *Nat. Hazards* **2016**, *85*, 19–37. [[CrossRef](#)]
13. Waqas, H.; Lu, L.; Tariq, A.; Li, Q.; Baqa, M.F.; Xing, J.; Sajjad, A. Flash Flood Susceptibility Assessment and Zonation Using an Integrating Analytic Hierarchy Process and Frequency Ratio Model for the Chitral District, Khyber Pakhtunkhwa, Pakistan. *Water* **2021**, *13*, 1650. [[CrossRef](#)]
14. Avtar, R.; Singh, C.K.; Shashtri, S.; Singh, A.; Mukherjee, S. Identification and analysis of groundwater potential zones in Ken–Betwa river linking area using remote sensing and geographic information system. *Geocarto Int.* **2010**, *25*, 379–396. [[CrossRef](#)]
15. Singh, C.K.; Shashtri, S.; Singh, A.; Mukherjee, S. Quantitative modeling of groundwater in Satluj River basin of Rupnagar district of Punjab using remote sensing and geographic information system. *Environ. Earth Sci.* **2010**, *62*, 871–881. [[CrossRef](#)]
16. Gaber, A.; Abdelkareem, M.; Abdelsadek, I.S.; Koch, M.; El-Baz, F. Using InSAR Coherence for Investigating the Interplay of Fluvial and Aeolian Features in Arid Lands: Implications for Groundwater Potential in Egypt. *Remote Sens.* **2018**, *10*, 832. [[CrossRef](#)]
17. Mallick, J.; Khan, R.A.; Ahmed, M.; Alqadhi, S.D.; Alsubih, M.; Falqi, I.; Hasan, M.A. Modeling Groundwater Potential Zone in a Semi-Arid Region of Aseer Using Fuzzy-AHP and Geoinformation Techniques. *Water* **2019**, *11*, 2656. [[CrossRef](#)]
18. Mukherjee, I.; Singh, U. Delineation of groundwater potential zones in a drought-prone semi-arid region of east India using GIS and analytical hierarchical process techniques. *CATENA* **2020**, *194*, 104681. [[CrossRef](#)]
19. Lettenmaier, D.P.; Alsdorf, D.; Dozier, J.; Huffman, G.J.; Pan, M.; Wood, E.F. In roads of remote sensing into hydrologic science during the WRR era. *Water Resour. Res.* **2015**, *51*, 7309–7342. [[CrossRef](#)]
20. Melese, T.; Belay, T. Groundwater Potential Zone Mapping Using Analytical Hierarchy Process and GIS in Muga Watershed, Abay Basin, Ethiopia. *Glob. Chall.* **2021**, *6*, 2100068. [[CrossRef](#)]
21. Abdelkareem, M.; El-Baz, F. Remote sensing of paleodrainage systems west of the Nile River, Egypt. *Geocarto Int.* **2016**, *32*, 541–555. [[CrossRef](#)]
22. Abdelkareem, M.; Gaber, A.; Abdalla, F.; El-Din, G.K. Use of optical and radar remote sensing satellites for identifying and monitoring active/inactive landforms in the driest desert in Saudi Arabia. *Geomorphology* **2020**, *362*, 107197. [[CrossRef](#)]
23. Roth, L.E.; Elachi, C. Coherent electromagnetic losses by scattering from volume in homogenities. *IEEE Trans. Antennas Propag.* **1975**, *23*, 674–675. [[CrossRef](#)]
24. Paillou, P.; Schuster, M.; Tooth, S.; Farr, T.; Rosenqvist, A.; Lopez, S.; Malezieux, J.-M. Mapping of a major paleodrainage system in eastern Libya using orbital imaging radar: The Kufrah River. *Earth Planet. Sci. Lett.* **2009**, *277*, 327–333. [[CrossRef](#)]
25. Saaty, T. A scaling method for priorities in hierarchical structures. *J. Math. Psychol.* **1977**, *15*, 234–281. [[CrossRef](#)]
26. Saaty, T.L. *The Analytic Hierarchy Process: Planning, Priority Setting, Resource Allocation*; McGraw-Hill: New York, NY, USA, 1980.
27. Razandi, Y.; Pourghasemi, H.R.; Neisani, N.S.; Rahmati, O. Application of analytical hierarchy process, frequency ratio, and certainty factor models for groundwater potential mapping using GIS. *Earth Sci. Inform.* **2015**, *8*, 867–883. [[CrossRef](#)]
28. Saaty, T.L. *Decision Making for Leaders: The Analytic Hierarchy Process for Decisions in a Complex World*; RWS Publications: Pittsburgh, PA, USA, 1990.
29. Yeh, H.-F.; Cheng, Y.-S.; Lin, H.-I.; Lee, C.-H. Mapping groundwater recharge potential zone using a GIS approach in Hualian River, Taiwan. *Sustain. Environ. Res.* **2016**, *26*, 33–43. [[CrossRef](#)]
30. Benjmel, K.; Amraoui, F.; Boutaleb, S.; Ouchchen, M.; Tahiri, A.; Touab, A. Mapping of Groundwater Potential Zones in Crystalline Terrain Using Remote Sensing, GIS Techniques, and Multicriteria Data Analysis (Case of the Ighrem Region, Western Anti-Atlas, Morocco). *Water* **2020**, *12*, 471. [[CrossRef](#)]
31. Murmu, P.; Kumar, M.; Lal, D.; Sonker, I.; Singh, S. Delineation of groundwater potential zones using geospatial techniques and analytical hierarchy process in Dumka district, Jharkhand, India. *Groundw. Sustain. Dev.* **2019**, *9*, 1002392. [[CrossRef](#)]
32. Kumar, V.A.; Mondal, N.C.; Ahmed, S. Identification of Groundwater Potential Zones Using RS, GIS and AHP Techniques: A Case Study in a Part of Deccan Volcanic Province (DVP), Maharashtra, India. *J. Indian Soc. Remote Sens.* **2020**, *48*, 497–511. [[CrossRef](#)]
33. Shaban, A.; Khawlie, M.; Abdallah, C. Use of remote sensing and GIS to determine recharge potential zones: The case of Occidental Lebanon. *Appl. Hydrogeol.* **2005**, *14*, 433–443. [[CrossRef](#)]
34. Rahmati, O.; Samani, A.N.; Mahdavi, M.; Pourghasemi, H.R.; Zeinivand, H. Groundwater potential mapping at Kurdistan region of Iran using analytic hierarchy process and GIS. *Arab. J. Geosci.* **2014**, *8*, 7059–7071. [[CrossRef](#)]
35. Achu, A.L.; Reghunath, R.; Thomas, J. Mapping of Groundwater Recharge Potential Zones and Identification of Suitable Site-Specific Recharge Mechanisms in a Tropical River Basin. *Earth Syst. Environ.* **2019**, *4*, 131–145. [[CrossRef](#)]
36. Abdalla, F.; Moubark, K.; Abdelkareem, M. Groundwater potential mapping using GIS, linear weighted combination techniques and geochemical processes identification, west of the Qena area, Upper Egypt. *J. Taibah Univ. Sci.* **2020**, *14*, 1350–1362. [[CrossRef](#)]

37. Pham, B.T.; Phong, T.V.; Nguyen, H.D.; Qi, C.; Al-Ansari, N.; Amini, A.; Ho, L.S.; Tuyen, T.T.; Yen, H.P.; Ly, H.B.; et al. A Comparative Study of Kernel Logistic Regression, Radial Basis Function Classifier, Multinomial Naïve Bayes, and Logistic Model Tree for Flash Flood Susceptibility Mapping. *Water* **2020**, *12*, 239. [CrossRef]
38. Youssef, A.M.; Pradhan, B.; Sefry, S.A. Flash flood susceptibility assessment in Jeddah city (Kingdom of Saudi Arabia) using bivariate and multivariate statistical models. *Environ. Earth Sci.* **2015**, *75*, 12. [CrossRef]
39. Moore, I.D.; Grayson, R.B.; Ladson, A.R. Digital terrain modelling: A review of hydrological, geomorphological, and biological applications. *Hydrol. Process.* **1991**, *5*, 3–30. [CrossRef]
40. Souissi, D.; Msaddek, M.H.; Zouhri, L.; Chenini, I.; El May, M.; Dlala, M. Mapping groundwater recharge potential zones in arid region using GIS and Landsat approaches, southeast Tunisia. *Hydrol. Sci. J.* **2018**, *63*, 251–268. [CrossRef]
41. Sharma, T.P.; Zhang, J.; Raj Khanal, N.; Prodhon, F.A.; Nanzad, L.; Zhang, D.; Nepal, P. A Geomorphic Approach for Identifying Flash Flood Potential Areas in the East Rapti River Basin of Nepal. *ISPRS Int. J. Geo-Inf.* **2021**, *10*, 247. [CrossRef]
42. Conoco. *Geological Map of Egypt, Scale 1:500,000*; The Egyptian General Petroleum Corporation: Cairo, Egypt, 1987.
43. O'Callaghan, J.F.; Mark, D.M. The extraction of drainage networks from digital elevation data. *Comput. Vis. Graph. Image Process.* **1984**, *28*, 323–344. [CrossRef]
44. Strahler, A.N. Quantitative analysis of watershed geomorphology. *Eos Trans. Am. Geophys. Union* **1957**, *38*, 913–920. [CrossRef]
45. Strahler, A.N. Quantitative geomorphology of drainage basins and channel networks. In *Handbook of Applied Hydrology*; Chow, V.T., Ed.; McGraw Hill Book Company: New York, NY, USA, 1964; Section 4II.
46. Shukla, G.; Tiwari, P.; Dugesar, V.; Srivastava, P.K. Estimation of evapotranspiration using surface energy balance system and satellite datasets. In *Agricultural Water Management Theories and Practices*; Srivastava, P.K., Gupta, M., Tsakiris, G., Quinn, N., Eds.; Academic Press: Cambridge, MA, USA, 2021; Chapter 9, pp. 157–183.
47. ALOS-2 (Advanced Land Observing Satellite-2; SAR Mission)/Daichi-2. Available online: <https://earth.esa.int/web/eoportal/satellite-missions/a/alos-2> (accessed on 15 November 2019).
48. Global PALSAR-2/PALSAR/JERS-1 Mosaic and Forest/Non-Forest Map. Available online: [https://www.eorc.jaxa.jp/ALOS/en/palsar\\_fnf/data/2017/map.htm](https://www.eorc.jaxa.jp/ALOS/en/palsar_fnf/data/2017/map.htm) (accessed on 15 November 2019).
49. Jensen, J.R. *Remote Sensing of the Environment: An Earth Resource Perspective*; Prentice-Hall: Englewood Cliffs, NJ, USA, 2000; p. 544.
50. Saaty, T.L. *Fundamentals of Decision Making and Priority Theory with the AHP*; RWS Publications: Pittsburgh, PA, USA, 1994.
51. Gannouni, S.; Gabtni, H. Structural Interpretation of Lineaments by Satellite Image Processing (Landsat TM) in the Region of Zahret Medien (Northern Tunisia). *J. Geogr. Inf. Syst.* **2015**, *7*, 119–127. [CrossRef]
52. Assatse, W.T.; Nouck, P.N.; Tabod, C.T.; Akame, J.M.; Biringanine, G.N. Hydrogeological activity of lineaments in Yaoundé Cameroon region using remote sensing and GIS techniques. *Egypt. J. Remote Sens. Space Sci.* **2016**, *19*, 49–60.
53. Berhanua, K.; Hatiye, S.D. Identification of Groundwater Potential Zones Using Proxy Data: Case study of Megech Watershed, Ethiopia Kibrit Gedam Berhanua, Samuel Dagalo Hatiye. *J. Hydrol. Reg. Stud.* **2020**, *28*, 100676. [CrossRef]
54. Ramu Mahalingam, B.; Vinay, M. Identification of ground water potential zones using GIS and Remote sensing Techniques: A case study of Mysore taluk-Karnataka. *Int. J. Geomat. Geosci.* **2010**, *5*, 2014.
55. Tehrany, M.S.; Pradhan, B.; Jebur, M.N. Flood susceptibility mapping using a novel ensemble weights-of-evidence and support vector machine models in GIS. *J. Hydrol.* **2014**, *512*, 332–343. [CrossRef]
56. Tehrany, M.S.; Pradhan, B.; Mansor, S.; Ahmad, N. Flood susceptibility assessment using GIS-based support vector machine model with different kernel types. *CATENA* **2015**, *125*, 91–101. [CrossRef]
57. Andualem, T.G.; Demeke, G.G. Groundwater potential assessment using GIS and remote sensing: A case study of Guna tana landscape, upper blue Nile Basin, Ethiopia. *J. Hydrol. Reg. Stud.* **2019**, *24*, 100610. [CrossRef]
58. Elewa, H.H.; Qaddah, A.A. Groundwater potentiality mapping in the Sinai Peninsula, Egypt, using remote sensing and GIS-watershed-based modeling. *Appl. Hydrogeol.* **2011**, *19*, 613–628. [CrossRef]
59. Ghorbani Nejad, S.; Falah, F.; Daneshfar, M.; Haghizadeh, A.; Rahmati, O. Delineation of groundwater potential zones using remote sensing and GIS-based data driven models. *Geocarto Int.* **2017**, *32*, 167–187. [CrossRef]
60. Pourtaghi, Z.S.; Pourghasemi, H.R. GIS-based groundwater spring potential assessment and mapping in the Birjand Township, southern Khorasan Province, Iran. *Appl. Hydrogeol.* **2014**, *22*, 643–662. [CrossRef]
61. Al-Abadi, A.M.; Shahid, S.; Ghalib, H.B.; Handhal, A.M. A GIS-Based Integrated Fuzzy Logic and Analytic Hierarchy Process Model for Assessing Water-Harvesting Zones in Northeastern Maysan Governorate, Iraq. *Arab. J. Sci. Eng.* **2017**, *42*, 2487–2499. [CrossRef]
62. Prasad, R.K.; Mondal, N.; Banerjee, P.; Nandakumar, M.V.; Singh, V.S. Deciphering potential groundwater zone in hard rock through the application of GIS. *Environ. Earth Sci.* **2007**, *55*, 467–475. [CrossRef]
63. Magesh, N.S.; Chandrasekar, N.; Soundranayagam, J.P. Delineation of groundwater potential zones in Theni district, Tamil Nadu, using remote sensing, GIS and MIF techniques. *Geosci. Front.* **2012**, *3*, 189–196. [CrossRef]
64. Pande, C.B.; Khadri, S.F.R.; Moharir, K.N.; Patode, R.S. Assessment of groundwater potential zonation of Mahesh River basin Akola and Buldhana districts, Maharashtra, India using remote sensing and GIS techniques. *Sustain. Water Resour. Manag.* **2017**, *4*, 965–979. [CrossRef]
65. Lentswe, G.B.; Lentswe, M. Delineation of potential groundwater recharge zones using analytic hierarchy process-guided GIS in the semi-arid Motloutse watershed, eastern Botswana. *J. Hydrol. Reg. Stud.* **2020**, *28*, 100674. [CrossRef]

66. Schumn, S.A. Evaluation of drainage systems and slopes in badlands at Perth Amboy, New Jersey. *Bull. Geol. Soc. Am.* **1956**, *67*, 597–646. [[CrossRef](#)]
67. Horton, R.E. Drainage-basin characteristics. *Trans. Am. Geophys. Union* **1932**, *13*, 350–361. [[CrossRef](#)]
68. Faniran, A. The index of drainage intensity—A provisional new drainage factor. *Aust. J. Sci.* **1968**, *31*, 328–330.
69. Strahler, A.N. Hypsometric analysis of erosional topography. *Bull. Geol. Soc. Am.* **1952**, *63*, 1117–1142. [[CrossRef](#)]
70. Davis, J.C. *Statics and Data Analysis in Geology*; Wiley: New York, NY, USA, 1975.
71. Brooks, H.E.; Stensrud, D.J. Climatology of Heavy Rain Events in the United States from Hourly Precipitation Observations. *Mon. Weather Rev.* **2000**, *128*, 1194–1201. [[CrossRef](#)]
72. Jaafarzadeh, M.S.; Tahmasebipour, N.; Haghizadeh, A.; Pourghasemi, H.R.; Rouhani, H. Groundwater recharge potential zonation using an ensemble of machine learning and bivariate statistical models. *Sci. Rep.* **2021**, *11*, 5587. [[CrossRef](#)] [[PubMed](#)]
73. Kotb, A.; Mosaad, S.; Kehew, A.E. Geophysical and hydrogeological applications for groundwater evaluation, east El-Minia area, upper Egypt. *J. Afr. Earth Sci.* **2021**, *184*, 104384. [[CrossRef](#)]
74. Abdelkareem, M.; El-Baz, F. Mode of formation of the Nile Gorge in northern Egypt: A study by DEM-SRTM data and GIS analysis. *Geol. J.* **2015**, *51*, 760–778. [[CrossRef](#)]
75. Priya, U.; Iqbal, M.A.; Abdus Salam, M.; Nur-E-Alam, M.; Uddin, M.F.; Islam, A.T.; Sarkar, S.K.; Imran, S.I.; Eh Rak, A. Sustainable Groundwater Potential Zoning with Integrating GIS, Remote Sensing, and AHP Model: A Case from North-Central Bangladesh. *Sustainability* **2022**, *14*, 5640. [[CrossRef](#)]
76. Todd, D.K.; Mays, L.W. *Groundwater Hydrology*, 3rd ed.; John Wiley & Sons: Hoboken, NJ, USA, 2013.
77. Vijith, H.; Dodge-Wan, D. Modelling terrain erosion susceptibility of logged and regenerated forested region in northern Borneo through the Analytical Hierarchy Process (AHP) and GIS techniques. *Geoenviron. Disasters* **2019**, *6*, 8. [[CrossRef](#)]
78. Pradhan, B. Groundwater potential zonation for basaltic watersheds Groundwater potential zonation for basaltic watersheds. *Cent. Eur. J. Geosci.* **2009**, *1*, 120–129.
79. Fagbohun, B.J. Integrating GIS and multi-influencing factor technique for delineation of potential groundwater recharge zones in parts of Ilesha schist belt, southwestern Nigeria. *Environ. Earth Sci.* **2018**, *77*, 69. [[CrossRef](#)]
80. Hong, Y.; Abdelkareem, M. Integration of remote sensing and a GIS-based method for revealing prone areas to flood hazards and predicting optimum areas of groundwater resources. *Arab. J. Geosci.* **2022**, *15*, 114. [[CrossRef](#)]
81. Ahmed, A.A.; Shabana, A.R. Integrating of remote sensing, GIS and geophysical data for recharge potentiality evaluation in Wadi El Tarfa, eastern desert, Egypt. *J. Afr. Earth Sci.* **2020**, *172*, 103957. [[CrossRef](#)]
82. Beven, K.J.; Kirkby, M.J. A physically based, variable contributing area model of basin hydrology/Un modele a base physique de zone d'appel variable de l'hydrologie du bassin versant. *Hydrol. Sci. J.* **1979**, *24*, 43–69. [[CrossRef](#)]
83. Chen, W.; Li, Y.; Tsangaratos, P.; Shahabi, H.; Ilia, I.; Xue, W.; Bian, H. Groundwater Spring Potential Mapping Using Artificial Intelligence Approach Based on Kernel Logistic Regression, Random Forest, and Alternating Decision Tree Models. *Appl. Sci.* **2020**, *10*, 425. [[CrossRef](#)]
84. Gheith, H.; Sultan, M. Construction of a hydrologic model for estimating Wadi runoff and groundwater recharge in the Eastern Desert, Egypt. *J. Hydrol.* **2002**, *263*, 36–55. [[CrossRef](#)]